



PHOTONICS Research

Lead–halide perovskites for next-generation self-powered photodetectors: a comprehensive review

CHANDRASEKAR PERUMAL VEERAMALAI,¹ SHUAI FENG,¹ XIAOMING ZHANG,^{1,5} S. V. N. PAMMI,² VINCENZO PECUNIA,³ AND CHUANBO LI^{1,4,6}

¹School of Science, Minzu University of China, Beijing 100081, China

²Department of Materials Science and Engineering, Chungnam National University, 34134 Daejeon, Republic of Korea

³Jiangsu Key Laboratory for Carbon-Based Functional Materials & Devices, Institute of Functional Nano & Soft Materials (FUNSOM), Joint International Research Laboratory of Carbon-Based Functional Materials and Devices, Soochow University, Suzhou 215123, China

⁴Optoelectronics Research Center, Minzu University of China, Beijing 100081, China

⁵e-mail: xmzhang@muc.edu.cn

⁶e-mail: cbli@muc.edu.cn

Received 5 February 2021; revised 17 March 2021; accepted 22 March 2021; posted 22 March 2021 (Doc. ID 418450); published 20 May 2021

Metal halide perovskites have aroused tremendous interest in optoelectronics due to their attractive properties, encouraging the development of high-performance devices for emerging application domains such as wearable electronics and the Internet of Things. Specifically, the development of high-performance perovskite-based photodetectors (PDs) as an ultimate substitute for conventional PDs made of inorganic semiconductors such as silicon, InGaAs, GaN, and germanium-based commercial PDs, attracts great attention by virtue of its solution processing, film deposition technique, and tunable optical properties. Importantly, perovskite PDs can also deliver high performance without an external power source; so-called self-powered perovskite photodetectors (SPPDs) have found eminent application in next-generation nanodevices operating independently, wirelessly, and remotely. Earlier research reports indicate that perovskite-based SPPDs have excellent photoresponsive behavior and wideband spectral response ranges. Despite the high-performance perovskite PDs, their commercialization is hindered by long-term material instability under ambient conditions. This review aims to provide a comprehensive compilation of the research results on self-powered, lead–halide perovskite PDs. In addition, a brief introduction is given to flexible SPPDs. Finally, we put forward some perspectives on the further development of perovskite-based self-powered PDs. We believe that this review can provide state-of-the-art current research on SPPDs and serve as a guide to improvising a path for enhancing the performance to meet the versatility of practical device applications. © 2021 Chinese Laser Press

<https://doi.org/10.1364/PRJ.418450>

1. INTRODUCTION

The innovation of functional materials with tunable optoelectronic properties will take essential positions in the development of fundamental and applied research fields. Metal halide perovskite materials with a typical crystal structure such as CaTiO_3 would evolve into an outstanding semiconductor counterpart to surpass all traditional materials in the optoelectronic field [1,2]. The general chemical formula of perovskites is ABX_3 , where “A” and “B” are two cations of very different sizes and “X” is an anion that bonds to both “A” and “B.” Progress has been achieved in synthesis, structural characterization, and investigations of physical properties of perovskite compounds in the form of three-dimensional (3D) bulk crystals, two-dimensional (2D) nanosheets, one-dimensional (1D) nanorods or nanowires, and zero-dimensional (0D) quantum dots (QDs) or nanocrystals [3]. Perovskite materials exhibit fas-

cinating and unique physical properties that have been extensively studied for both practical applications and theoretical modeling [4]. In this sense, perovskite materials’ potential applications are varied and include uses in sensors, fuel cells, solar cells, photodetectors (PDs), memory devices, lasers, and spintronic applications [5,6]. Among the above, PDs are an essential optoelectronic component found to have a wide range of applications, both in industry and daily life, including astronomy, surveillance, robotics, smartphones, and environmental monitoring [7,8]. Until recent years, PDs have been made up of inorganic semiconductors such as Si, InGaAs, and GaN, which are used to detect light in the visible range (450–800 nm), infrared (900–1700 nm) range, and UV range (250–400 nm), respectively [4]. Despite the fact that these PD technologies possess mature and authentic fabrication processes, their widespread application and commercialization are impeded by complex and expensive manufacturing processes,

mechanical inflexibility to current smart systems, and the requirement of high driving voltage. For example, the photoresponsivities of commercially available Si-, Ge-, and InGaAs-based PDs are usually around few A/W under high bias voltages (5–200 V). Therefore, an alternative is needed to overcome the existing problems; searching for novel material is a motivation.

Meanwhile, in the near future, the era of the Internet of Things (IoT) will integrate sensors and objects with networks and solely play an eminent role in world economic development [9]. With the predictable trending, the smart sensor network, as an inevitable component of the IoT, will become a key field in deciding the future development of information technology [10]. Understandably, the smart sensor network requires a great amount of electric energy for sustainable and maintenance-free operation. However, such a huge power cannot be provided due to the huge number of sensor networks and the complexity of replacing batteries every time. Therefore, wireless devices should be self-powered without using batteries.

In general, a conventional PD needs to be operated by an external power source; typically, it is the battery. However, such independent power supplies are not compatible with a future intelligent sensor system in the following ways: (1) the material used for the battery construction is likely to be highly hazardous to the ecosystem; and (2) the requirement of battery recycling has to be considered in terms of cost for an integrated PD network. Therefore, independent, sustainable, and maintenance-free PDs can be operated by an built-in power source or by extracting power from the surrounding environment. So, a PD operated under self-biasing mode is called a self-powered PD.

In recent years, self-powered electronic devices (in other words, PDs) have received extensive attention along with the rapid development of smart systems and wearable electronics in daily life, for example, smart homes, bioimaging, health monitoring, and optical communications [11]. Generally, self-powered PDs are classified as Schottky diodes, p-n junction diodes, and metal–semiconductor–metal (MSM) diodes based on device structure and junction formation [7,11–16]. By now, there have been numerous reports on SPPDs, which can sense from the deep ultraviolet (DUV) to far infrared regions (FIRs). Though the performance metrics are very adequate, currently all the proposed self-powered perovskite photodetectors (SPPDs) are not suitable for commercial applications due to the complexity of device fabrication, the cost factor, and the mechanical rigidity, which make them difficult to integrate with electronic components. With the benefit of longer carrier diffusion length and high charge carrier mobility, high absorption coefficient ($\alpha \approx 10^5 \text{ cm}^{-1}$), and high defect tolerance, perovskite materials could be the best choice for self-powered PDs. These excellent optoelectronic properties allow detection of light to be realized within the perovskite layers, even with 100–200 nm thin films, which is ideal for high-resolution imaging applications, whereas conventional technologies such as silicon-based imaging devices require micrometer-range thick layers. Furthermore, the solution processed manufacturing and the ease of fabrication process of perovskite layers at low temperatures compared with conventional complementary metal–oxide–semiconductor (CMOS) technology make it attractive for future development of electronics field.

Therefore, these additional advantages of perovskite materials are potentially attractive for large-area manufacturing at low-cost production, which provides fabrication of self-powered PDs on flexible polymer substrates.

There have been a considerable number of review papers that separately covered perovskite-based PDs, nanoscale self-powered PDs, and self-powered UV PDs [17–19]. However, a comprehensive review focused mainly on self-powered perovskite-based-PDs, specifically on fabrication technique, device performance in-terms of photoresponsivity, specific detectivity, response speed is lacking in the literature. This review is mainly focused on self-powered perovskite-based PDs. First, we introduce the working principle and basic mechanism of self-powered PD systems in two types of modes: the photovoltaic (PV) mode and the integrated-self powered system. Then, we summarize the recent progress on self-powered perovskite-based PDs by sectioning the structure of perovskites such as bulk crystal structure (3D), nanosheets (2D), nanowires or microwires (1D), and QDs or nanocrystals (0D). Besides, we introduce flexible self-powered perovskite photodetectors (SPPDs). Despite the considerable advancement in the field, there are several key challenges ahead to face in the further development of SPPDs. Therefore, we have provided a survey of challenges and opportunities in the last section.

2. GENERAL PROPERTIES OF ORGANIC-INORGANIC PEROVSKITE AND ALL-INORGANIC PEROVSKITE MATERIALS

The perovskite materials have a canonical stoichiometric formula of ABX_3 , where A is a monovalent organic or inorganic cation such as methylammonium (MA^+ , CH_3NH_3^+), formamidinium [FA^+ , $\text{HC}(\text{NH}_2)_2^+$], or Cesium (Cs^+), B is a divalent metal cation (typically Pb^{2+} , or Sn^{2+}), and X is halide anions (I, Br, Cl) [20,21]. The crystal structure consists of a 3D network of corner-sharing $[\text{BX}_6]^{4-}$ octahedra with a 12-fold coordinated A cation occupying the site in the middle of the cube surrounded by 8 octahedra. Although there are several ABX_3

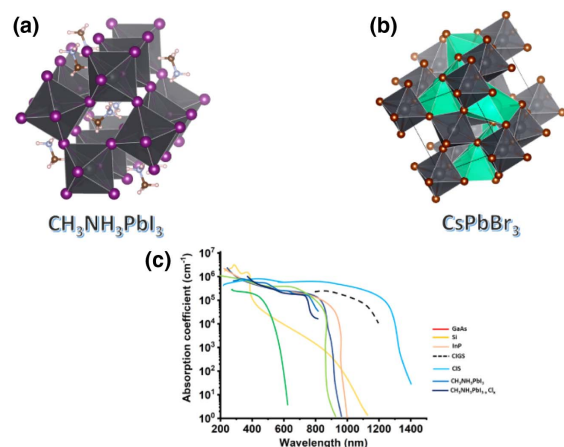


Fig. 1. (a), (b) Schematic crystal structure of representative perovskite materials $\text{CH}_3\text{NH}_3\text{PbI}_3$ and CsPbBr_3 , simulated from Vesta.3 Software; (c) comparative optical absorption behavior of semiconducting materials. Reproduced from Ref. [6] with permission. Copyright 2014, Springer Nature.

Table 1. Basic Characteristic Physical Parameters of Perovskite Materials

Material	Diffusion Length (μm)	Lifetime (μs)	Mobility ($\text{cm}^2 \text{V}^{-1} \text{s}^{-1}$)	Trap Density (cm^{-3})	Reference
MAPbI ₃ thin film	0.1–1	0.01–1	1–10	10^{15} – 10^{16}	[25]
MAPbI ₃ single crystal	2–8	0.5–1	24–105	10^{10}	[26]
CsPbBr ₃ thin film	≥ 9.2	–	41.3	–	[27]
CsPbBr ₃ single crystal	5.5	25	52	1.1×10^{10}	[28,29]

structures with various A cations, only Cs⁺, MA⁺ and FA⁺ meet the requirement for the formation of stable 3D perovskite by fulfilling the Goldschmidt tolerance factor. Among them, the MAPbI₃ perovskite structure is very popular and the most studied one [Fig. 1(a)]. MAPbI₃ has a suitable bandgap of ~ 1.55 eV, which matches the wavelength of ~ 800 nm, making it a competitive light-absorbing material for solar cells and photosensors [22]. Through the modulation of halogen component (I⁻, Br⁻, Cl⁻) within the crystal structure, the bandgap and spectra of perovskite material can even be adjusted [3]. For instance, doping of lighter halogen ions gives a larger exciton binding energy (E_b). The binding energy of the electron-hole pairs in excitons, a primary photoexcited species created in the absorption process, is vital in the operation of photoelectric devices. The exciton binding energy (E_b) of the low-temperature orthorhombic phase of MAPbI₃ is only 16 meV, while that of the room-temperature tetragonal phase is 2 meV [23]. This small E_b makes the excited-state properties of perovskites comparable with inorganic semiconductors (e.g., Si, 15.0 meV) [24], which is beneficial for their application in PDs and solar cells. Besides, perovskites also possess some other fascinating properties such as piezoelectricity, a high absorption coefficient, and long charge diffusion length. The typical key physical parameters such as diffusion length, carrier lifetime, mobility, and trap density for both polycrystalline thin-film structure and bulk crystals are summarized in Table 1. Specifically, as shown in Fig. 1(c), the absorption properties of perovskite are consistent with direct band-gap solar cell materials reported earlier. These attractive features make perovskites ideal candidates for optoelectronic devices, such as solar cells, light-emitting diodes (LEDs), PDs, and laser diodes.

Despite the remarkable device performance offered, organic-inorganic perovskites suffer from degradation by air, moisture, temperature, electric field, and light exposure (detailed analysis is provided in challenges and perspectives section later) [30,31]. Particularly, the organic cation clusters [CH₃NH³⁺, FA⁺, CH(NH₂)²⁺, etc.] in the organic-inorganic hybrid lead halide perovskite are extremely sensitive to the environmental humidity and oxygen content, leading to problems such as poor environmental stability and poor thermal stability [32,33]. Furthermore, the perovskite material intrinsically suffers from issues such as migration of ions and the appearance of hysteresis in the electrical characteristics [34,35]. The making of stable functional devices is greatly restricted by these issues. Therefore, a stable perovskite requires a partial replacement organic counterpart with more stable cations such as long-chain organic cations or inorganic elements such as cesium (Cs) and rubidium (Rb) [36–38]. A representative all-inorganic perovskite CsPbBr₃ is a direct band-gap semiconductor with low trap state density, high carrier mobility, long electron-hole diffusion

length, etc., and it also has some excellent optical characteristics such as high quantum yield, strong light absorption, high luminous efficiency, and adjustable luminous wavelength (see Table 1) [1].

3. PERFORMANCE PARAMETERS OF PHOTODETECTORS

Here, some very important performance parameters to describe the characteristics of a PD can be summarized as follows.

Responsivity. The responsivity is given as the ratio of the output current or voltage to the power of the input light signal, and the unit is A/W or V/W.

$$R = \frac{I_p}{PA}, \quad (1)$$

where $I_p = I_{\text{light}} - I_{\text{dark}}$, P is the incident power density, and A is the effective device area.

Specific detectivity. D^* is a key figure of merit to reflect the sensitivity of a device. In general, the specific detectivity of the PD is related to the noise inversely. It is defined in terms of responsivity R as

$$D^* = \frac{(A\Delta f)^{1/2}}{i_n} R = R \sqrt{\frac{A}{2qI_d}}, \quad (2)$$

where R is the responsivity in A W^{-1} , A is the effective device area, I_d is the dark current, and q is the coulombic charge of the electron (1.6×10^{-19} C).

External quantum efficiency (EQE): EQE is the ratio of the output number of electrons/holes to the number of incident photons, indicating the conversion efficiency of PDs from photons to charges. It is given as follows:

$$\text{EQE} = \frac{Rhc}{q\lambda}, \quad (3)$$

where h , c , q , and λ denote Planck's constant, the speed of light, elementary electron charge, and wavelength, respectively.

Noise equivalent power (NEP): NEP is the signal power that produces a signal-to-noise ratio (SNR) to be equal to 1, representing the minimum impinging optical power that a PD can distinguish from the noise. It can be written as

$$\text{NEP} = \frac{(A\Delta f)^{1/2}}{D^*} = \frac{i_n}{R}, \quad (4)$$

where A is the effective device area, Δf is the electrical bandwidth, and i_n is the noise current.

Linear dynamic range (LDR): It describes a light intensity range in which the current response of the PD is linearly proportional to the light intensity, and it can be calculated by

$$\text{LDR} = 20 \log \frac{J_{\max} - J_d}{J_{\min} - J_d}, \quad (5)$$

where J_{\max} is the upper photocurrent, J_{\min} is the lower photocurrent, and J_d is the dark current. Detecting both the weak and strong light is required for a high LDR PD.

Response speed: Rise time (t_r) and decay time (t_d) are defined as the time within which photocurrent increases from 10% to 90% and drops from 90% to 10% of its maximum value.

4. BRIEF INTRODUCTION ON SPPDS: CLASSIFICATION BY WORKING MECHANISM

Energy consumption is one of the important aspects considered for modern electronic devices which needs further development to achieve a better sustainable future. This is equally true for commercially available PDs. In recent years, there have been numerous reports on SPPDs operated from the DUV to the near-infrared (NIR) under zero bias voltage. The SPPDs are categorized into two types based on energy source feeding as follows: (1) PV effect-based PDs (Schottky junction and heterojunction) and (2) PDs with integrated self-powered systems.

A. PV Effect-Based Self-Powered PDs

Fundamentally, PDs operate on the basis of the transition of electrons from the lower energy state to the higher energy state under photonic illumination. At present, commercial PDs are operated based on photoconductive (PC) mode and PV mode. PC mode detectors identify the light signal by detecting the change of resistance across the photoactive material under illumination. In contrast, PV-type PDs utilize the built-in electric field in heterojunction or Schottky junctions to separate the photogenerated electron–hole pairs. Thus, the need for an external bias is omitted, so the device is termed a self-powered PD. Figure 2(a) illustrates the charge separation under the PV effects in a heterojunction. Since the required built-in electrical fields generally exist in junctions between materials with different work functions, PV-type PDs could be feasibly constructed from doping or simple hybrid materials combinations [39].

Apart from SPPDs based on the p-n heterojunction, PDs based on the Schottky junction can also operate without external power sources owing to the PV effect. Furthermore, compared to p-n heterojunction PDs, Schottky-type PDs exhibit ultrarapid response time, high photosensitivity, and low-cost fabrication, which is highly preferable for future applications. Generally, a built-in electric field, which separates the photogenerated electron–hole pairs and gives rise to circuit current, is formed due to the electron's spontaneous diffusion caused by the work function difference between contact metal and semiconductor. Unfortunately, the surface state of semiconductors could seriously affect the diffusion process. Therefore, to achieve high performance, a great endeavor is required to optimize the stability and quality of the Schottky contact. Up to the present, several investigations of self-powered Schottky-type PDs made from different semiconductors have been reported [18,40–45].

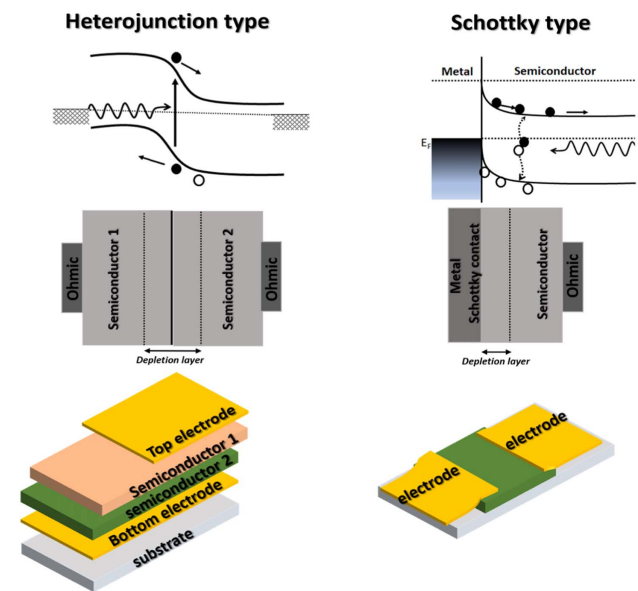


Fig. 2. Schematic diagrams of working principle of SPPDs in PV mode: heterojunction type (left side) and Schottky type (right side).

B. Integrated Nanopower Source-Based Self-Powered PDs

For the realization of self-powered PDs in PV mode, the following aspects should be considered: (1) SPPDs can not only detect the signals but also must be powered by the detected signals; (2) the photogenerated electron–hole pairs are usually separated by the built-in potential difference provided by the junction-based multilayer structures, which often involve complicated, time-consuming, and uneconomic device fabrication processes [46]; (3) more importantly, the material choice of this kind of device is limited due to issues such as lattice mismatch, surface states, and band alignment [47–49]. These issues not only increase the system size but also greatly limit mobility and independence [50]. In this regard, a miniaturized, uninteruptible energy source is necessary to power up the PD.

The nanogenerator (NG) is a new technique, first proposed by Wang in 2007, that utilizes mechanical and thermal energies produced by human body motion and then converts into electrical energy [51]. Generally, NGs can be classified into three types based on electricity generation modes: the triboelectric generator (TENG), the piezoelectric NG (PENG), and the pyroelectric NG (PYENG). A TENG is an energy-harvesting device that converts mechanical energy into electrical energy by a combination of triboelectric effect and electrostatic induction. A PENG is a device capable of converting external kinetic energy into electrical energy via motion by piezoelectric materials. The conversion of external thermal energy into electrical energy is adopted for designing PYENGs. Among the above, TENG is a compatible nanoenergy source that is frequently used to back up the electronic devices and has drawn more attention. These NGs are widely used as the micronanoenergy sources for self-powered sensors. However, integration of NGs with sensor devices is always challenging, but further

development of NG-based self-powered sensors is extremely attractive.

5. PEROVSKITE-BASED-SELF-POWERED PDS

A. Single-Crystal Perovskite PDs

The single-crystal perovskites possess many unique advantages over polycrystalline thin-film structures, such as high purity, fewer grain boundaries, and enhanced thermal and moisture stabilities. Notably, in a single crystal, low trap density contributes to high carrier mobility and long carrier diffusion lengths, resulting in highly sensitive PDs. High-purity perovskite single crystals have been prepared by several methods reported earlier such as inverse temperature crystallization (ITC) [52], antisolvent vapor-assisted crystallization [26], top-seed solution growth [53], bottom-seeded solution growth [54], and solvent acidolysis crystallization [55].

By adopting the above-mentioned techniques, there have been numerous reports on the successful synthesis of high-quality single crystals. Recently, the fabrication of single-crystal

heterostructures has attracted great interest in the construction of SPPDs. For example, the $\text{CH}_3\text{NH}_3(\text{MA})\text{PbBr}_3/\text{CH}_3\text{NH}_3(\text{MA})\text{PbI}_x\text{Br}_{3-x}$ heterojunction single crystal was prepared via ITC and successfully used to fabricate self-powered PDs by Cao *et al.* [56]. The post-synthesized MAPbBr_3 single crystal was vertically dipped into the oversaturated $\text{MAPbI}_3/\text{GBA}$ solution for 2 s using a tweezer and then dried in a nitrogen atmosphere. The crystal was annealed at 100°C for 5–10 min until it was completely dry, and then core-shell $\text{MAPbBr}_3/\text{MAPbI}_x\text{Br}_{3-x}$ heterojunction was obtained. The synthesis process is illustrated in Fig. 3(a). The as-fabricated PD with device configuration $\text{FTO}/\text{MAPbBr}_3/\text{MAPbI}_x\text{Br}_{3-x}/\text{Au}$ exhibits peak photoresponsivity up to 11.5 mA W^{-1} under 450 nm illumination at 0 V bias [Fig. 3(b)]. The device's performance is a result of accelerated exciton dissociation with the help of the built-in electric field in the heterojunction. Photogenerated electron–hole pairs are separated by a strong local electric field arising from the band bending at the junction; the electrons are injected into

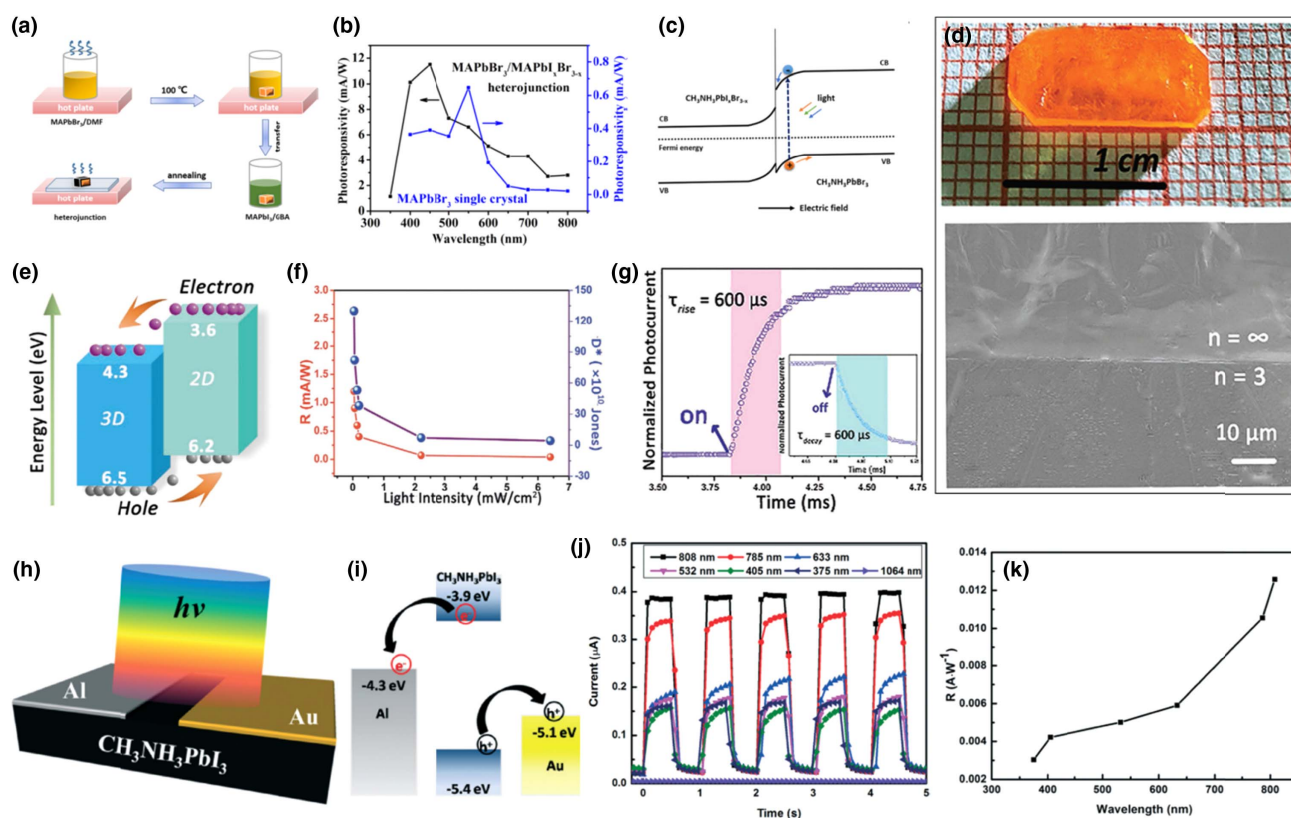


Fig. 3. (a) Preparation process of the $\text{MAPbBr}_3/\text{MAPbI}_x\text{Br}_{3-x}$ heterojunction; (b) responsivity of $\text{APbBr}_3/\text{MAPbI}_x\text{Br}_{3-x}$ and single crystal MAPbBr_3 PDs at zero bias under the incident light with wavelengths of 350–800 nm and 400–800 nm, respectively; (c) schematic energy level diagram at the $\text{MAPbBr}_3/\text{MAPbI}_x\text{Br}_{3-x}$ junction under irradiation. Reproduced with permission from Ref. [56]. Copyright 2016, American Institute of Physics. (d) Photographic image of the as-grown heterostructure single crystal (top); SEM image of the heterostructure interface (bottom). (e) Band diagram of the $(4\text{-AMP})(\text{MA})_2\text{Pb}_3\text{Br}_{10}/\text{MAPbBr}_3$ heterostructure detector; (f) plots of the R and D^* as a function of light intensity; (g) response speed of $(4\text{-AMP})(\text{MA})_2\text{Pb}_3\text{Br}_{10}/\text{MAPbBr}_3$ heterostructure device at rise edges and fall edges. Reproduced with permission from Ref. [57]. Copyright 2020, Wiley-VCH. (h) Schematic illustration of the Au–Al electrodes separated by $30 \mu\text{m}$ on MAPbI_3 single crystal; (i) schematic illustration of the working mechanism for Schottky junction based on asymmetric electrodes; (j) photocurrent response of $\text{Au}/\text{MAPbI}_3/\text{Al}$ device at different wavelengths; (k) spectral photoresponsivity of MAPbI_3 single crystal PD. Reproduced with permission from Ref. [58]. Copyright 2016, Royal Society of Chemistry.

MAPb_{1-x}Br_{3-x}, and the holes are transferred to MAPbBr₃, leading to a remarkable photocurrent at zero bias [Fig. 3(c)].

Similarly, Zhang *et al.* have reported on a vertical 2D/3D perovskite heterostructure (4-AMP) (MA)₂Pb₃Br₁₀/MAPbBr₃ [4-AMP-4-(aminomethyl) piperidinium], featuring a well-defined interface and high crystalline quality [57]. The photographic image of single-crystal heterostructure and corresponding cross-sectional field emission scanning electron microscopy (FESEM) image are shown in Fig. 3(d). Electrical transport measurements demonstrate that the (4-AMP) (MA)₂Pb₃Br₁₀/MAPbBr₃ heterostructure can form a vertical diode with obvious current rectification behavior and photocurrent generation characteristics. Benefiting from the built-in electrical field at the junction [Fig. 3(e)], PDs based on those millimeter-thickness heterostructure crystals exhibit high performance in self-driven operation mode, including fast response time (600/600 μs), and high detectivity ($\approx 10^{12}$ Jones) [Figs. 3(f) and 3(g)].

Besides heterojunction-based SPPDs, the Schottky junction is another choice that can also generate a built-in electric field due to the Fermi energy difference between metal and semiconductor junction. The recent emergence of a new approach to making a Schottky junction by using asymmetric electrodes is fascinating for its simplicity and efficiency. Ding *et al.* fabricated a self-powered PD based on a CH₃NH₃PbI₃ single crystal by implementing asymmetric Au–Al electrodes [58]. The authors simply deposited Au and Al on the surface of the perovskite single crystal in planar geometry [Fig. 3(h)]. A 30 μm gap was selected between the electrodes, which is far less than

the charge diffusion length of 175 μm in a single crystal [53]. The Schottky barrier was closely related to the work function of the metal and the electron affinity of the semiconductor. In other words, the electrons moved from the conduction-band minimum of a semiconductor to contacted metal (the holes move from valence-band maximum to contacted metal) to get a balanced Fermi level. The metal Al (work function -4.3 eV) was chosen to form a high barrier and Au (work function -5.1 eV) to form a low barrier, as schematically shown in Fig. 3(i). Accordingly, the electric field from Au to Al is built into the device. The as-fabricated device shows excellent photoresponse behavior in the broad wavelength region from 808 to 1064 nm, as shown in Fig. 3(j), and the spectral photoresponsivity of the device is depicted in Fig. 3(k). Moreover, the device exhibits photoresponsivity of 0.24 A W⁻¹ at the lowest incident intensity of 1 × 10⁻⁸ W cm⁻², with a fast rise and decay time of 71 and 112 μs, respectively. Similarly, all-inorganic perovskite single crystals also have shown comparable photodetective performance metrics as that of hybrid perovskite single crystals. For example, Saidaminov *et al.* reported a self-powered PD using a CsPbBr₃ single crystal synthesized via the inversion temperature crystallization technique [Fig. 4(a)] [28]. The device was fabricated in a vertical structure with configuration Au/CsPbBr₃/Pt and shows specific detectivity of 1.7 × 10¹¹ Jones and a photoresponsivity of 28 mA W⁻¹ at 550 nm illumination under self-powered mode [Figs. 4(b) and 4(c)]. Such an asymmetric electrode-induced self-powered PD has been realized in various single crystals and has been proposed as the phenomenon behind the enhanced PD performance [59].

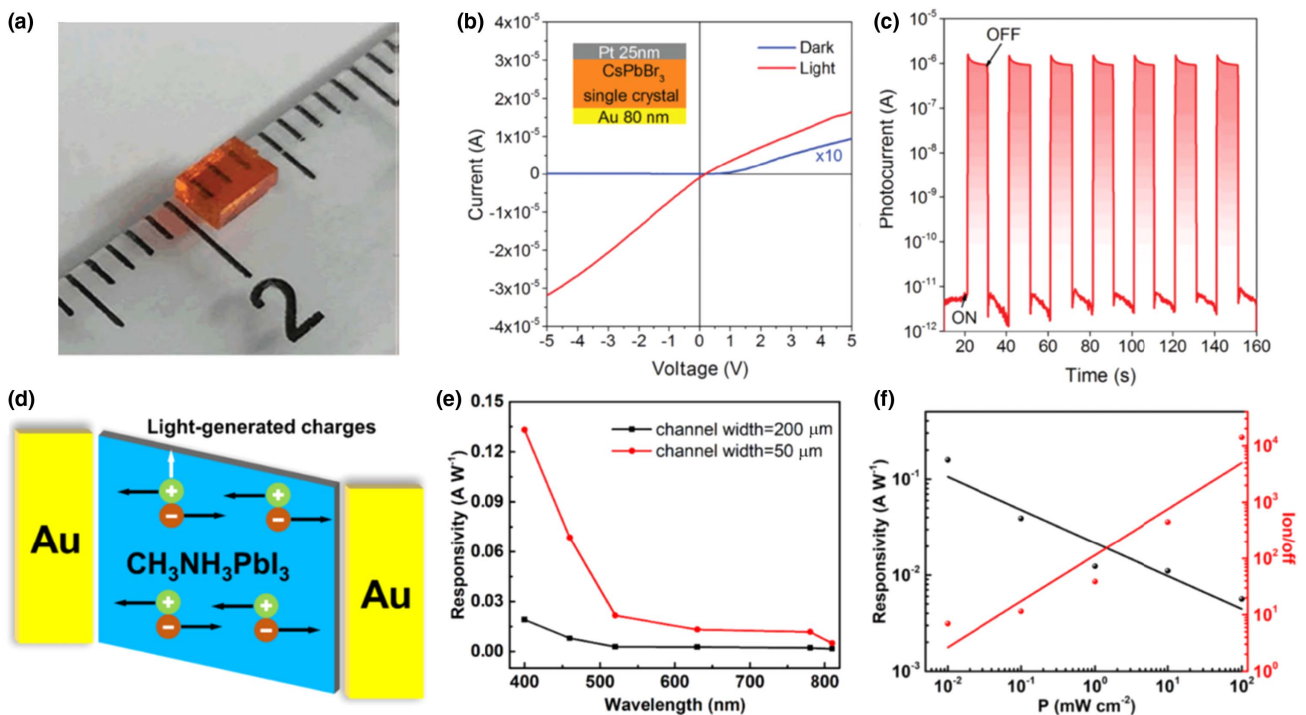


Fig. 4. (a) Photographic image of CsPbBr₃ single crystal; (b) I - V curve of device Au/CsPbBr₃/Pt in dark and under illumination; (c) photoresponse of device Au/CsPbBr₃/Pt under light pulses measured under zero bias. Reproduced with permission from Ref. [28]. Copyright 2017, Wiley-VCH. (d) Carrier separation transmission diagram of the device based on CH₃NH₃PbI₃ single crystal PD; (e) variation of light responsivity of devices with different channel widths; (f) dependence of responsivity and on-off ratio on the light intensity. Reproduced with permission from Ref. [60]. Copyright 2021, Elsevier.

Though the concept of the Schottky junction is considered for designing asymmetric electrode configuration-self-powered PDs, the intrinsic mechanism for charge carrier transport in a single crystal was interpreted differently.

In the $\text{CH}_3\text{NH}_3\text{PbI}_3$ crystal, a $[\text{PbI}_6]$ octahedral structure is constituted by Pb and I atoms, and CH_3NH_3^+ is located in an octahedron cavity. The distortion of the $[\text{PbI}_6]$ octahedron results in the Pb_2^+ not occupying the center of the octahedron, and so the crystal symmetry is destroyed, inducing a spontaneous polarization in the perovskite. The spontaneous polarization of the $\text{CH}_3\text{NH}_3\text{PbI}_3$ unit cell and the ordered arrangement of the unit cell in the single crystal provide the possibility of the single crystal achieving self-powered PDs. For instance, a self-powered PD in a MAPbI_3 single crystal was reported by Zhang *et al.*, where the symmetric electrode is fabricated in $\text{Au}/\text{MAPbI}_3/\text{Au}$ [60]. However, from the device structure of $\text{Au}/\text{MAPbI}_3/\text{Au}$, if the MAPbI_3 crystal is non-polar, two Schottky junctions with the same barrier height will be formed at both ends of the device. Such a device has no built-in electric field and cannot realize the self-powered characteristic, which is contrary to the experimentally observed self-powered phenomenon. Therefore, the ferroelectric spontaneous polarization exists in the MAPbI_3 single crystal, which is responsible for the self-powered mechanism of PDs. Briefly, the photogenerated carriers in ferroelectric materials are separated by the depolarization field associated with spontaneous polarization and collected by the Au electrodes at both ends of the device to generate the potential difference. The process of carrier movement is shown in Fig. 4(d). Moreover, Fig. 4(e) shows that the photoresponsivity of the device greatly depends on the channel size, i.e., increased channel size could effectively increase the illumination area of the device and enhance the photocurrent, while the carrier collection efficiency is simultaneously reduced, and then the responsivity of the device is decreased. Without external bias, the device exhibited the maximum responsivity of 0.16 A W^{-1} and the specific detectivity of 5.86×10^{11} Jones with a fast response time.

B. Nanostructured Perovskite PDs

Recently, low-dimensional nanostructures have been extensively studied as a potential building block to construct efficient PDs. Compared with bulk materials, low-dimensional nanoscale materials, with their large surface areas and possible quantum confinement effect, exhibit distinct electronic, optical, chemical, and thermal properties [61]. One should consider that poor structural stability and chemical stability remain major concerns for the practical application of halide perovskites. So, the high surface-area-to-volume ratio of nanostructured perovskite can increase the impact of surface properties on the chemical properties and phase stability. However, nanostructures of halide perovskites can exhibit enhanced structural and chemical stability owing to a surface energy effect and surface ligand functionalization [62]. Therefore, a large variety of perovskite nanostructures, such as QDs/nanocrystals, nanowires/nanorods, and nanosheets, were successfully synthesized, which could be effectively applicable in PDs [3,63].

Among the various nanostructured perovskite materials, colloidal QDs (CQDs) exhibit the unique characteristics of the size-dependent optical bandgap, size tunability, large extinction

coefficient, high photoluminescence quantum yield (PLQY), and multiple exciton generation; all these characteristics make them suitable candidates for optoelectronic devices. Generally, two types of methods are widely used to synthesize perovskite QDs: (i) ligand assisted reprecipitation (LARP) and (ii) the hot injection method. It can be inferred from earlier results that highly luminescent perovskite QDs are predominantly applied for light-emitting diodes (LEDs) [64,65]. However, subsequent studies suggested that perovskite QDs have great potential application in high-performance PDs [66]. Due to the small size of QDs, the formation of a large number of grain boundaries is unavoidable. These grain boundaries are a source of charge traps with a large density that make for low carrier mobility for the nanocrystal (NC) thin films. Thus, the preparation of dense NC films is particularly important, and the optimization strategy for the preparation of high-quality perovskite films with fewer defects is always required. For example, Chandrasekar *et al.* proposed a perovskite CQD-based self-powered PD by providing asymmetric electrode configuration [50]. The authors prepared the high-quality MAPbI_3 CQDs by LARP combined with the ultrasonication technique. The schematic illustration of the preparation technique for MAPbI_3 NCs is presented in Fig. 5(a), and the high resolution transmission electron microscopy (HRTEM) image of the as-synthesized CQDs as shown in Fig. 5(b) adequately demonstrated the formation of NCs in spherical shape with uniform size distribution. Furthermore, a simple photodiode $\text{ITO}/\text{MAPbI}_3/\text{Ag}$ is fabricated, as shown in Fig. 5(c). The J - V curve confirms the existence of the PV effect due to work function variation of indium tin oxide (ITO) (4.8 eV) and Ag (4.2 eV), as presented in Fig. 5(d). Moreover, the device exhibits an offset voltage of 0.64 V under 808 nm light illumination with a high photoresponsivity of 1.42 A W^{-1} and a specific detectivity of 1.77×10^{13} Jones. The self-powered PDs respond to the NIR wavelength of 808 nm with a rise and decay time of 279 and 341 ms, respectively [Fig. 5(e)]. The PDs show the broad photoresponse behavior from visible wavelength to NIR wavelength, which is uncommon in perovskite-based PDs.

Apart from the Schottky junction PD, perovskite QDs are used as a photosensitive layer in multilayer junctions to realize heterojunction-based self-powered PDs. For example, Imran *et al.* proposed a trilayer PD with device structure $\text{ITO}/\text{ZnO}/\text{CdS}/\text{CsPbBr}_3/\text{Au}$ [67]. To reduce the interfacial charge carriers' recombination and the charge transport resistance, CdS nanorods are sandwiched between a $\text{ZnO}/\text{CsPbBr}_3$ interface. The cross-sectional FESEM image of the device is shown in Fig. 5(f). The typical I - V curve of the device represents the PV effect by the formation of an open-circuit voltage of 0.13 V, as shown in Fig. 5(g). The device performance could be explained based on the band diagram, as illustrated in Fig. 5(h). In the trilayer device, built-in potentials are induced at both the $\text{CdS}/\text{CsPbBr}_3$ and ZnO/CdS interfaces, and both CsPbBr_3 and CdS nanorod layers can absorb the incident light. This doubly formed built-in potential in the trilayer device results in more efficient separation of photogenerated carriers and then more efficient drift to electrodes at zero bias. Overall, the self-powered trilayer PD shows photoresponsivity of 86 mA W^{-1} and specific detectivity of

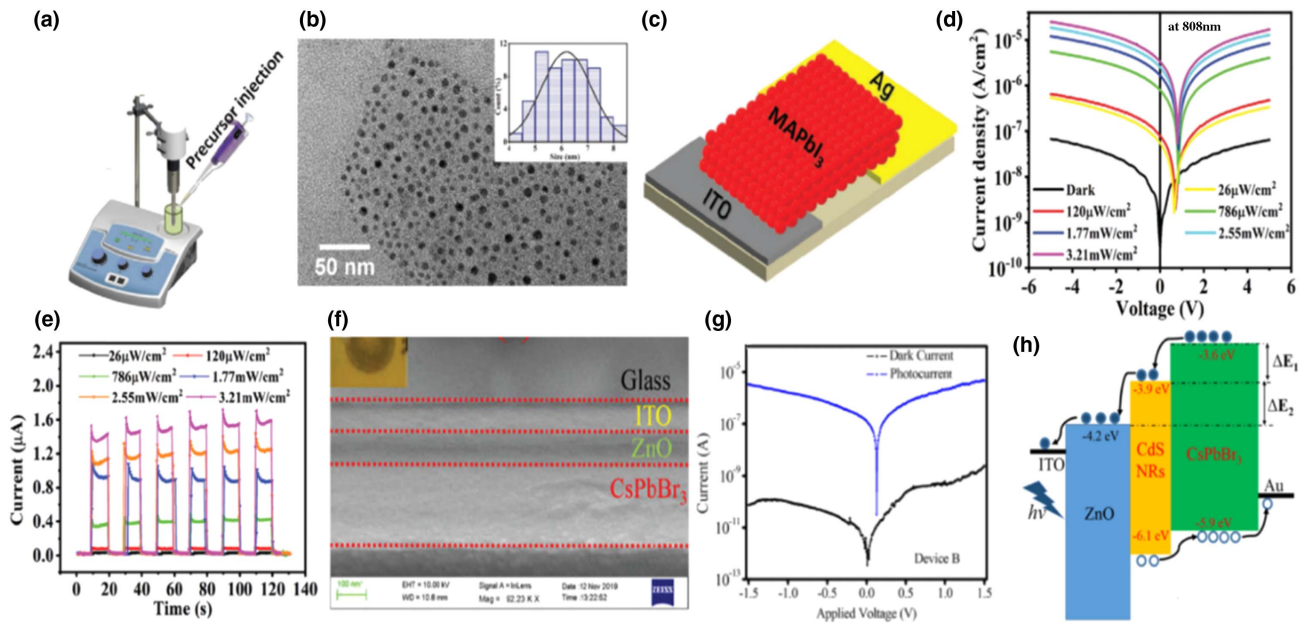


Fig. 5. (a) Schematic illustration of MAPbI₃ NC synthesis; (b) TEM image of MAPbI₃ NCs (the inset shows MAPbI₃ nanocrystal size distribution plot); (c) schematic diagram of the MAPbI₃ NC based self-powered PD; (d) J - V curves of the MAPbI₃ NC-based self-powered PD under 808 nm illumination; (e) photocurrent versus time for the PD under light on/off cycles at 0 V under 808 nm illumination. Reproduced with permission from Ref. [50]. Copyright 2020, Wiley-VCH. (f) Cross-sectional SEM image of ITO/ZnO(70 nm)/CdS(150 nm)/CsPbBr₃(200 nm)/Au trilayer PDs; (g) I - V curve of trilayer PD device in dark and under 85 $\mu\text{W cm}^{-2}$ 405 nm illumination; (h) potential charges generation and transportation process under 85 $\mu\text{W cm}^{-2}$ 405 nm illumination illustrated by band diagram. Reproduced with permission from Ref. [67]. Copyright 2020, Institute of Physics.

6.2×10^{11} Jones with the rise and decay time of 0.3 s and 0.25 s, respectively.

Similar to 0D perovskite QDs, 1D perovskite materials also found potential application in PDs owing to their high sensitivity, reduced recombination rate, and quick charge transfer characteristics. Until now, a great number of the studies carried out by researchers on the fabrication of PDs used various perovskite nanowires/nanorods, microwires, microtubes, etc. [68–73]. However, nanowire/nanorod-based self-powered PDs have seldom been reported in the literature. The reasons can be summarized as follows: (i) complicated fabrication process of nanowires (NWs) as a device structure and poor reproducibility; (ii) the photocurrents of the PDs based on aligned NWs or a single NW with MSM structure are very low due to the limited light absorption cross section or the large channel length between the metal electrodes; (iii) a phenomenon of the p-n junction and the Schottky junction required for achieving self-powered PDs is very complicated in individual NW PDs or aligned NW PDs due to difficulties of p or n doping in perovskites and tedious nanowire manipulation [68,74].

Recently, Zhou *et al.* demonstrated the fabrication of CsPbBr₃ NW self-powered PDs with a vertical p-i-n structure in which CsPbBr₃ NWs are grown by a solution process and halide exchange [68]. The detailed fabrication process is depicted in Fig. 6(a). To fabricate the self-powered PD, the as-grown NWs are sandwiched between SnO₂ electron selective layers (ESLs) and poly(triarylamine) (PTAA) hole selective layers (HSLs), and to realize a perfect p-i-n structure, poly(methyl methacrylate) (PMMA) is coated on the NWs before the deposition of the PTAA layer [Fig. 6(b)]. The charge carrier

generation and transportation across the device are illustrated by the band diagram shown in Fig. 6(c). The as-fabricated PD shows a good response to 473 nm light illumination, with a rising time of 0.4 ms and a decaying time of 0.43 ms [Fig. 6(d)]. Also, the self-powered PD exhibits photoresponsivity of 0.3 A W⁻¹ and specific detectivity of 1.0×10^{11} Jones [Fig. 6(e)]. Similarly, self-powered PDs based on PDPP3T and P3HT conjugated polymer integrated with CsPbBr₃ nanowire were reported by Cao *et al.* [69]. The CsPbBr₃ NWs are fabricated by imprinting a DVD-R disc on spin-coated CsPbBr₃ thin films and subsequently, a conjugated polymer layer is deposited to realize the bulk heterojunction PD [Figs. 6(f) and 6(h)]. The as-fabricated CsPbBr₃ NW arrays are highly aligned and perfectly crystallized, as shown in Fig. 6(g). This hybrid bulk heterojunction device shows broad photoresponse behavior in the UV-Vis-NIR region, and the value of R (>0.2 A W⁻¹) and D^* ($>1 \times 10^{13}$ Jones) is achieved in the spectral range from 350 to 500 nm, with the peak values of 0.25 A W⁻¹ and 1.2×10^{13} Jones, respectively, at the wavelength of 350 nm. Besides, R (>2 mA W⁻¹) and D^* ($>1 \times 10^{11}$ Jones) are achieved in the spectral range from 300 to 880 nm [Fig. 6(i)]. Moreover, the photocurrent of the device only shows <10% degradation, even after continuous white-light soaking for 21 h. Particularly, the device can maintain >90% photocurrent and retain high reproducibility after exposure to ambient atmosphere for 4 weeks [Fig. 6(j)].

Another fascinating perovskite nanostructure is 2D perovskite material (material with a thickness of a few nanometers or less), which includes nanosheets, nanoplates, and nanoflakes. The PDs based on 2D perovskite materials can exhibit a high

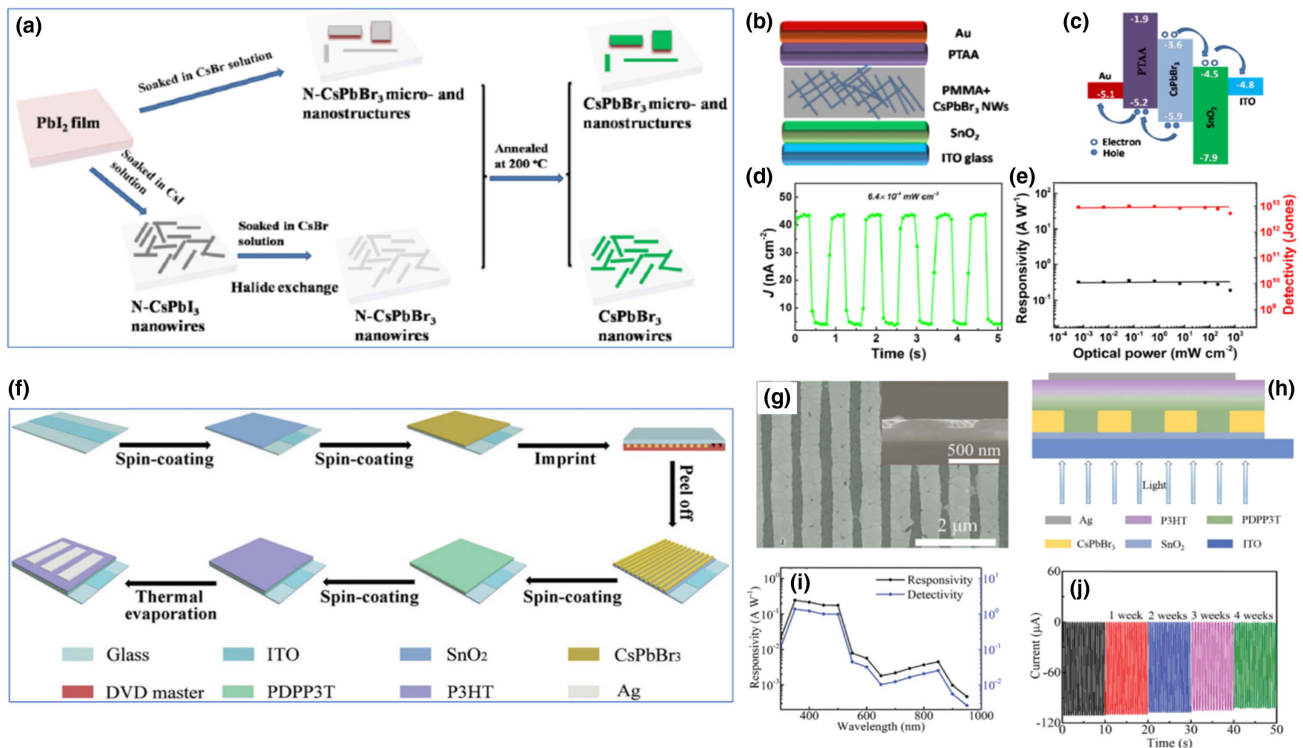


Fig. 6. (a) Schematic illustration of the synthesis process of the CsPbBr₃ NWs and CsPbBr₃ micro- and nanostructures; (b) schematic illustration of the perovskite NW PD; (c) energy band diagram of the perovskite NW PD. (d) J - t curve at the light intensity of $6.4 \times 10^{-4} \text{ mW cm}^{-2}$; (e) responsivity and detectivity of the device under various optical power. Reproduced with permission from Ref. [68]. Copyright 2018, Elsevier. (f) Schematic illustration of the fabrication process of the P3PCS PD; (g) CsPbBr₃ nanowire array; (h) schematic of device structure; (i) responsivity and detectivity curves of P3PCS device; (j) long-term photoresponse curves of P3PCS device under 100 mW cm^{-2} white light at 0 V. Reproduced with permission from Ref. [69]. Copyright 2019, Wiley-VCH.

photoresponse and superior flexibility owing to their strong quantum confinement and unique morphology. Previous studies focused on the synthesis of high-quality 2D perovskite by solution-processing and vapor-phase methods. Gui *et al.* reported the synthesis of CsPbBr₃ microplates by space-confined growth at low temperatures [Fig. 7(a)] [75]. The authors fabricated a vertically configured ITO/CsPbBr₃ MPs/Au PD, as shown in Fig. 7(b), and the device exhibits a rapid response speed of 75 μs and a very low dark current of 2 pA at zero bias. Moreover, the device shows the specific detectivity of $>10^{12}$ Jones and a linear dynamic range (LDR) equal to 137 dB, with excellent thermal and moisture stability [Figs. 7(c) and 7(d)]. Unlike the solution phase synthesis, the vapour phase method provides highly crystallized perovskite material and avoids the formation of grain boundary and surface defects. The minimized grain boundary and defects are highly required characteristics for enhanced charge carrier transport. Tian and coworkers demonstrated the fabrication of self-powered PDs using CVD-grown CsPbBr₃ microcrystals (MCs), where microcrystals are sandwiched between GaN and ZnO [Fig. 7(e)] [76]. The self-powered PD shows detectivity (D^*) of 10^{14} Jones, on/off ratio of up to 10^5 , peak responsivity (R) of 89.5 mA/W, and enhanced stability at the incident wavelength of 540 nm [Fig. 7(f)]. The PD enables the fast photoresponse speed of 100 μs (rise time) and 140 μs (decay time). Zhou *et al.* demonstrated high-quality CsPbBr₃ MCs synthesized through the

ITC technique [Fig. 7(g)] [77,78]. The device was fabricated in a vertical configuration with SnO₂ as the ESL and Spiro-MeOTAD as the HSL, as shown in Fig. 7(h). The as-fabricated self-powered all-inorganic CsPbBr₃ perovskite MC thick-film PDs show improved performance characteristics, with responsivity and detectivity of 0.206 A W⁻¹ and 7.23×10^{12} Jones, respectively.

C. Polycrystalline Thin-Film Perovskite PDs

Polycrystalline perovskite thin films could be possibly produced by adopting various strategies such as solvent annealing, thermal annealing, solvent engineering, atmospheric control, chemical vapor deposition, vacuum flash-assisted solution processing, and the use of additives [20,79–84]. These strategies have mostly been applied in fabricating high-efficiency perovskite solar cells and also in fabricating perovskite film PDs. The earlier studies revealed that the preparation process of perovskite polycrystalline thin films is simple and compatible with different configurations of PDs [85–87]. In addition, the formation of polycrystalline thin films on any arbitrary substrates such as glass, mica, and plastics is also very feasible. Nevertheless, a large number of studies were carried out in polycrystalline perovskite-based self-powered PDs. Dou *et al.* first reported solution-processed high-performance PDs based on CH₃NH₃PbI_{3-x}Cl_x films using the p-i-n vertical structure [p refers to the hole transport layer (HTL), i is the intrinsic

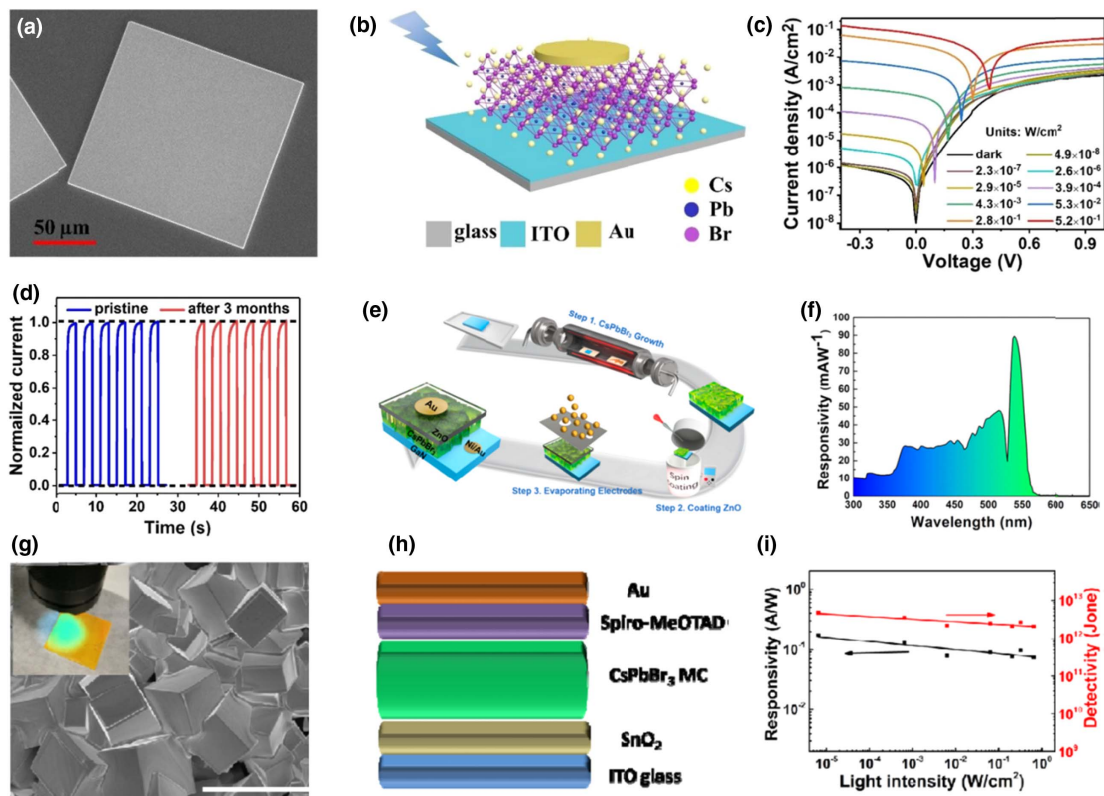


Fig. 7. (a) SEM image of CsPbBr₃ microplatelets shows sharp edge and smooth surface morphology. (b) Schematic layout of the perovskite CsPbBr₃ microplatelets PD based on vertical Schottky junction structure; (c) I - V characteristics of the CsPbBr₃ microplatelets PD under 405 nm light illumination with different density; (d) normalized I - t curves of CsPbBr₃ microplatelets PD with long-term storage without encapsulation. Reproduced with permission from Ref. [75]. Copyright 2020, Royal Society of Chemistry. (e) Schematic of fabricating process of the CsPbBr₃ microcrystal-based PD; (f) room temperature spectral responsivity curves of the CsPbBr₃ microcrystal-based PD at 0 V bias. Reproduced with permission from Ref. [76]. Copyright 2019, American Chemical Society. (g) SEM image of CsPbBr₃ microcrystal perovskite film. The inset is a digital photograph of the perovskite film under 365 nm purple flashlight. (h) Schematic illustration of the CsPbBr₃ microcrystal perovskite PD; (i) power-dependent R and D^* CsPbBr₃ microcrystal perovskite PD under 0 V bias. Reproduced with permission from Ref. [77]. Copyright 2019, American Chemical Society.

layer, and n is the electron transport layer (ETL)] photodiode inverted device configuration [Fig. 8(a)] [85]. Based on this design, the as-fabricated solution-processed self-powered PD exhibits large detectivity approaching 10^{14} Jones, an LDR over 100 dB, and a fast photoresponse with 3-dB bandwidth up to 3 MHz [Fig. 8(b)]. Compared to the solution-phase synthesis of perovskite thin-film structures, vapor phase growth provides high-quality thin films and can facilitate large area deposition of perovskite films with reduced grain boundaries. So, Pammi *et al.* fabricated MAPbI_{3-x}Cl_x films by CVD technique on NiO_x buffered FTO glass substrates [86]. The uniform, highly crystallized thin films [Fig. 8(c)] were used to fabricate self-powered PDs, as shown in Fig. 8(d). The as-fabricated device responds from the UV to the red region with the figure of merit value, photoresponsivity of 112 A W^{-1} and specific detectivity of 3.5×10^{14} Jones [Fig. 8(e)]. Moreover, the PD showed excellent operating stability in both light illumination and moisture, as presented in Fig. 8(f). Liu *et al.* have developed a sequential evaporation technique to fabricate high-quality CsPbBr₃ thin films [87]. The evaporated thin film possesses much higher crystallinity, phase purity, and larger grain size with fewer grain

boundaries, which is required for better charge transport properties in the device [Fig. 8(g)]. A self-powered PD is fabricated using CsPbBr₃ thin film as the photoactive layer, as shown in Fig. 8(h), where PMMA layer modification reduces trap states and leakage current pathways. The final device structure exhibits an on/off ratio of 3.5×10^4 , with a fast response time of 3.8 μs . The calculated R and D^* of the PMMA-modified PDs are 0.11 A W^{-1} and 4.4×10^{11} Jones. The as-fabricated CsPbBr₃ detectors also present superior stability after being stored in ambient air for over 1000 h. Bao *et al.* reported a self-powered PD by spin-coated CsPbI₂ thin film, as shown in Fig. 8(i) [88]. The as-fabricated device shows clear PV behavior with reduced dark current [Fig. 8(j)]. Moreover, the device exhibited a high average photoresponsivity of 280 mA W^{-1} and specific detectivity of 9.7×10^{12} Jones. Also, as shown in Fig. 8(k), the PD shows much better ambient stability with only 7% and 13% degradation on the device responsivity after more than 2000 h.

The stability of perovskite PDs, as well as the selection of photoactive material, is the most important issue taken into consideration while designing the structure of PDs. Li *et al.* demonstrated the fabrication of Cs_xDMA_{1-x}PbI₃ thin films

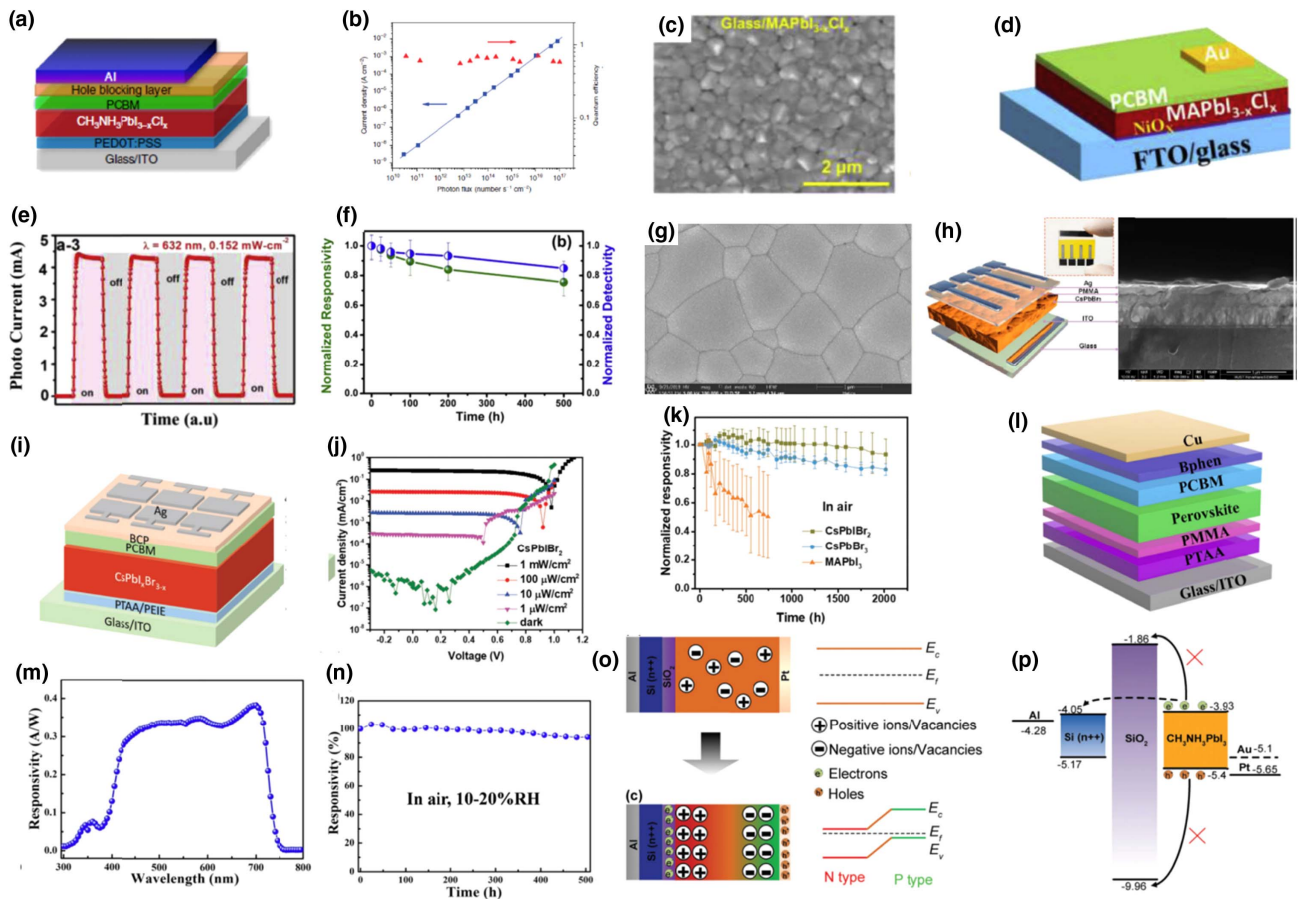


Fig. 8. (a) Device structure of the hybrid perovskite PD; (b) LDR of the PD with the device structure ITO/PEDOT:PSS/CH₃NH₃PbI_{3-x}Cl_x/PCBM/PFN/Al. The PD has a large LDR of 4100 dB. Reproduced with permission from Ref. [85]. Copyright 2014, Springer Nature. (c) SEM image of MAPbI_{3-x}Cl_x thin films on glass substrate; (d) schematic representation of a photodetector device configuration; (e) transient photocurrent properties of device under illumination at 632 nm; (f) long-term photo stability illuminated under 1000 μW/cm² with different intervals up to 500 h. Reproduced with permission from Ref. [86]. Copyright 2020, Elsevier. (g) SEM image of PMMA-modified CsPbBr₃ film; (h) schematic and cross-sectional SEM image of the as-fabricated PD with a structure of ITO/CsPbBr₃/PMMA/Ag. Reproduced with permission from Ref. [87]. Copyright 2020, Royal Society of Chemistry. (i) Schematic structure of PD based on all-inorganic perovskite CsPbI₂Br_{2-x}; (j) current density-voltage (*I*-*V*) curves of CsPbI₂Br₂-based PDs under dark and illumination of 450 nm monochrome light with intensity of 1 μW/cm² to 1 mW/cm²; (k) photoresponsivity evolution of PDs based on inorganic perovskite CsPbI₂Br_{2-x} and hybrid perovskite MAPbI₃ in air ambient condition without encapsulation. Reproduced with permission from Ref. [88]. Copyright 2018, Wiley-VCH. (l) Schematic illustration of as-fabricated self-powered PD based on Cs_xDMA_{1-x}PbI₃ perovskite films; (m) responsivity spectrum of the self-powered PD based on the film with CsI/DMAPI₃ molar ratio of 1:2 in the precursor at 0 V; (n) variation of spectral responsivity with time of the self-powered PD in air (10%–20% RH) at a bias voltage of 0 V under 532 nm illumination. Reproduced with permission from Ref. [89]. Copyright 2020, Elsevier. (o) Disordered state of ions under dark (upper) and mobile ions accumulated at the opposite interfaces under illumination due to the light-induced self-poling effect (lower), resulting in the built-in electric field; (p) energy band schematics of the MOS structure under dark before contact. Reproduced with permission from Ref. [90]. Copyright 2019, Royal Society of Chemistry.

by the solution-processing technique [89]. Instead of PbI₂, DMAPbI₃ [DMA⁺ = dimethylammonium, (CH₃)₂NH₂⁺] is chosen to react with CsI, which can enhance the room-temperature phase stability of resultant Cs-based perovskite films. A self-powered PD has been designed, as indicated in Fig. 8(l), which shows broad photoresponse from 300 to 750 nm, with high specific detectivity (>1×10¹³ Jones) [Fig. 8(m)]. Above all, the device shows excellent long-term stability in the air due to an increased tolerance factor by the introduction of DMA⁺; in other words, DMA⁺ prevents the spontaneous transformation of CsPbI₃ at room temperature [Fig. 8(n)].

In perovskite-based optoelectronic devices, ion migration is one of the interesting concepts to be investigated to understand unusual phenomena such as current-voltage hysteresis, switchable PV effect, and light-induced self-poling effect [35,91,92]. Pang and coworkers investigated the self-poling effect in perovskite thin films by designing the PD in a metal-oxide-semiconductor (MOS) structure [90]. The device with structure Si/SiO₂/CH₃NH₃PbI₃ showed excellent self-powered photoresponse characteristics and exhibited an excellent on/off ratio of 10⁵ with a bias of 0 V and a fast response time of 25.8 ms. The authors explained the “self-biasing” by the concept of self-poling effect as follows. When no bias is applied,

the mobile ions within the perovskite layer show electrical disorder in the dark, and the perovskite has a uniform Fermi level, as shown in Fig. 8(o) (upper side). Under illumination, the built-in electric field is formed when the positive ions/vacancies accumulate at the perovskite/SiO₂ interface and the negative ions/vacancies accumulate at the perovskite/Pt interface due to the preset built-in potential caused by band bending in the asymmetrical device [Fig. 8(o) (lower side)]. The typical band diagram elucidated from XPS spectra is shown in Fig. 8(p) and clearly explains the charge transport properties across the device.

D. Integrated Nanopower System-Based PDs

Recently, self-powered optoelectronic systems with an integrated energy supplying unit have attracted more attention, as their energy module converts environmental energy into electrical energy to operate the functional device without an additional energy cost. For instance, Su *et al.* designed self-powered PDs that utilize joint properties of the photoelectric effect and triboelectric effect of MAPbI₃ perovskite material [93]. The PD device consists of two friction layers, where the top layer is a Cu electrode with an elastic buffer layer and the bottom layer is composed of MAPbI₃/TiO₂/FTO [Fig. 9(a)]. The device exhibits a responsivity of 7.5 V W⁻¹, a rapid response time (<80 ms), and broad detection ranges from the UV to the visible regions. The mechanism of this PD is mainly due to the change of light-induced surface charge density. When an external force brings the top copper electrode into repeated contact with the perovskite layer in a periodic way, triboelectric charges of opposite signs on the contact surfaces induce an oscillating open-circuit voltage (V_{oc}) between the two electrodes. It was found that the variation of voltage

amplitude (V_{oc}) upon illumination increases as the light intensity increases. For example, voltage amplitude decreases to 35.5% upon solar illumination of 100 mW cm⁻², as shown in Fig. 9(b). Hsiao *et al.* designed another PD structure, in which a TENG is coupled with a perovskite PD, as shown in Fig. 9(c) [94]. In the typical PD structure, the photogenerated charge carriers are separated by the potential created by the TENG. Notably, the photocurrent and response time of the PD are found to be enhanced by triboelectricity. Before illumination, the perovskite PD is treated with triboelectric charge and the two electrodes (Au and ITO) are full of positive/negative charges provided by the TENG [Fig. 9(d)]. Under illumination, the lower Schottky barrier makes the photogenerated holes migrate to the Au/perovskite interface, leaving behind the unpaired electrons in the perovskite/ITO interface and contributing to the photocurrent. The generation of surface charges on the Au and ITO electrodes due to the application of TENG results in an enhanced photocurrent and subsequent photoresponse. The clear response of the photocurrent by the TENG is shown in Fig. 9(e), which demonstrates that triboelectricity can effectively improve the photoresponse of the perovskite PD in the on-off switching of light illumination. The updated progress in perovskite-based SPPDs is provided in Table 2.

6. FLEXIBLE SELF-POWERED PEROVSKITE-BASED PDS

The ultra-flexible, ultrafast (<20 ms), wearable, and flexible PDs are the highly studied research field due to their compatibility with a variety of emerging areas such as flexible, stretchable, wearable, portable, and printed optoelectronics. Combined with transparent features, flexible devices can be

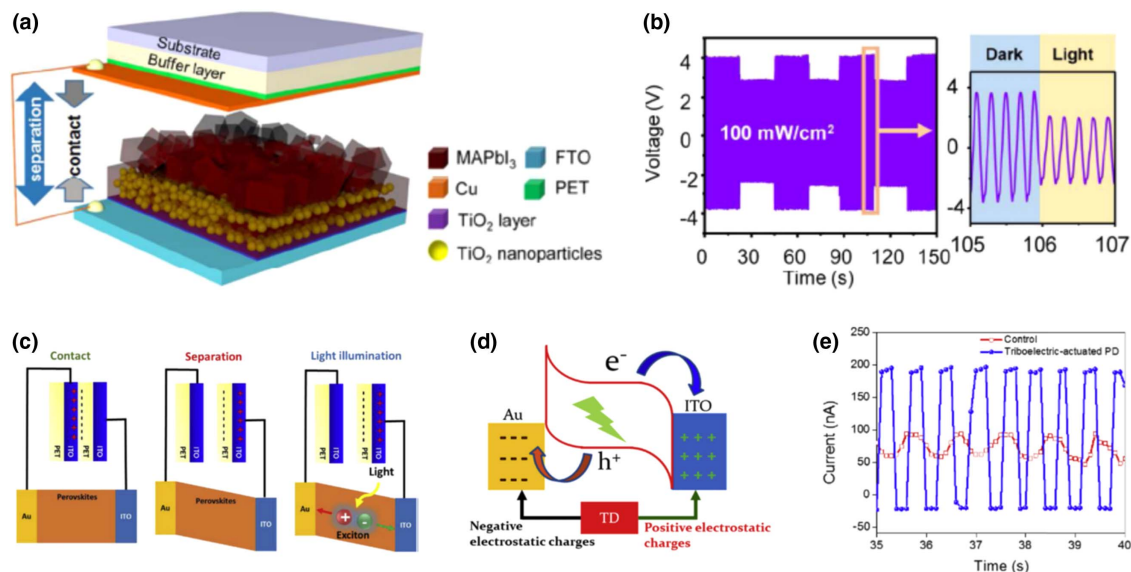


Fig. 9. (a) Device structure of self-powered PD with MAPbI₃ as the photosensitive and triboelectric layer; (b) change of V_{oc} upon repeated illumination that varies in intensity at 100 mW cm⁻². Reproduced with permission from Ref. [93]. Copyright 2015, American Chemical Society. (c) Schematic of a triboelectric-assisted perovskite PD showing charge carrier separation assisted by the triboelectric charges created by the TENG; (d) schematic diagram and the working principle of the (+) triboelectric-assisted perovskite PD; (e) transient photoresponse of the triboelectric-actuated perovskite PD (blue) and perovskite PD without assistance of triboelectricity (red) under alternating on-off laser light (50 mW) illumination with a 3 Hz chopping frequency. Reproduced with permission from Ref. [94]. Copyright 2019, Elsevier.

Table 2. Summary of Key Parameters of Perovskite-Based SPPDs

Device Structure	Physical Mechanism for Self-Mode (Junction)	Response		D^* (Jones)	τ_r/τ_f	Reference
		Wavelength (nm)	R (mA W ⁻¹)			
ZnO NRs-Spiro-MeOTAD	PV (heterojunction)	470 nm	6.5	Not mentioned	4/10 ms	[95]
CH ₃ NH ₃ PbBr ₃ /CH ₃ NH ₃ PbI _x Br _{3-x}	PV (heterojunction)	450 nm	11.5	Not mentioned	2.3/2.76 s	[57]
Au/CH ₃ NH ₃ PbI ₃ /Al	PV (Schottky)		240	Not mentioned	71/112 μ s	[59]
ITO/ZnO:CsPbBr ₃ /Ag	PV (Schottky)	405 nm	11.5	Not mentioned	0.409/0.017 s	[96]
Au/CsPbBr ₃ /Pt	PV (Schottky)	550 nm	28	1.7×10^{11}	230/60 ms	[28]
MoS ₂ /CH ₃ NH ₃ PbI ₃	PV (heterojunction)		60	not mentioned	2149/899 ms	[97]
ITO/PTAA/PEIE/CsPbI _x Br _{3-x} /PCPM/Ag	PV (p-i-n structure)	525 nm	280	9.7×10^{12}	20 ns	[90]
PS - CH ₃ NH ₃ PbI ₃	Electric field poling	Visible light	610	1.5×10^{13}	13 ms/14 ms	[98]
ZnONRs/CsPbBr ₃	PV (heterojunction)	Visible light	300	1.15×10^{13}		[99]
PtSe ₂ /Cs:FAPbI ₃	PV (heterojunction)	808 nm	117.7	2.91×10^{12}	70/60 ns	[100]
ITO/SnO ₂ /CsPbBr ₃ /PTAA/Au	PV (heterojunction)	473 nm	206	7.23×10^{12}	30/39 μ s	[80]
CsPbBr ₃	PV (p-i-n structure)	473 nm	300	1×10^{13}	0.4/0.43 ms	[70]
ITO/SnO ₂ /CsPbBr ₃ /SpiroMeOTAD/Au	PV (heterojunction)	473 nm	172	4.8×10^{12}	0.14/0.12 ms	[79]
PVP-CsPbI ₃	PV (heterojunction)	400–700 nm	100	1×10^{12}	5.7/6.2 μ s	[101]
P3HT-PDPP3T/CsPbBr ₃ /SnO ₂	Photovoltaic (heterojunction)	300–950 nm	250	1.2×10^{13}	111/306 μ s	[71]
CH ₃ NH ₃ PbI ₃	PV (heterojunction)	400 nm	250	1.53×10^{11}	110/72 ms	[102]
Carbon-CH ₃ NH ₃ PbI ₃	PV (heterojunction)	White light	1.3	8.2×10^{11}	200/500 ms	[103]
Al/Si/SiO ₂ /CH ₃ NH ₃ PbI ₃ /Pt	Light-induced self-poling effect	White light	Not mentioned	8.8×10^{10}	25.8/0.62 ms	[94]
GaN/CsPbBr ₃ MCs/ZnO	PV (heterojunction)	540 nm	89.5	$\sim 10^{14}$	100/140 μ s	[78]
CsBi ₃ I ₁₀ /silicon	PV (heterojunction)	820 nm	178.7	4.99×10^{10}	73/36 μ s	[104]
PdSe ₂ /FA _{1-x} Cs _x PbI ₃	PV (heterojunction)	800 nm	313	$\sim 10^{13}$	3.5/4 μ s	[105]
FTO/TiO ₂ /CsPbBr ₃ /carbon	PV (heterojunction)	520 nm	350	1.94×10^{13}	0.58 μ s/–	[106]
FTO/c-TiO ₂ /Cs _{0.05} MA _{0.16} FA _{0.79} Pb(I _{0.9} Br _{0.1}) ₃ /Spiro/Au	PV (heterojunction)	625 nm	520	8.8×10^{12}	19/21 μ s	[107]
ITO/PTAA/PMMA/Cs _x DMA _{1-x} PbI ₃ /PCPM/Bphen/Cu	PV (heterojunction)	532 nm	380	1×10^{13}	558 ns/–	[91]
ITO/CH ₃ NH ₃ PbI ₃ /Ag	PV (Schottky)	808 nm	1.42×10^3	1.77×10^{13}	279/341 ms	[51]
ITO/CsPbBr ₃ /PMMA/Ag	PV (Schottky)	450 nm	110	4.4×10^{11}	3.8/4.6 μ s	[89]
ITO/MAPbI ₃ :CuSCN/PCBM/BCP/Ag	PV (heterojunction)	640 nm	370	1.06×10^{12}	5.02/5.50 μ s	[108]
FTO/NiO _x /MAPbI _{3-x} /PCPM/Au	PV (heterojunction)	632 nm	112×10^3	3.5×10^{14}	0.23/0.38 s	[88]
ITO/ZnO/CdS/CsPbBr ₃ /Au	PV (heterojunction)	405 nm	86	6.2×10^{11}	0.3/0.25 s	[109]
ITO/SnO ₂ /CH ₃ NH ₃ PbI ₃ /Spiro-OMeTAD/Ag	PV (heterojunction)	720 nm	473	1.35×10^{13}	0.35/0.18 ms	[110]
Au/CH ₃ NH ₃ PbI ₃ /Au	PV (Schottky)	400 nm	160	5.89×10^{11}	150/50 ms	[62]
FTO/PEI/CsPbI ₃ /carbon	PV (Schottky)	520 nm	320	3.74×10^{12}	-/1.21 μ s	[111]
FTO/TiO ₂ /CsPbBr ₃ /carbon	PV (heterojunction)	405 nm	350	3.83×10^{13}	-/1.46 μ s	[112]
(4-AMP)(MA) ₂ Pb ₃ Br ₁₀ /MAPbBr ₃	PV (heterojunction)	405 nm	1.19	1.26×10^{12}	600/600 μ s	[58]
ITO/CsPbBr ₃ /Au	PV (Schottky)	500 nm	208	$\sim 10^{12}$	75/70 μ s	[77]
Au/CH ₃ NH ₃ PbI ₃ /Au	TENG	White light	196 V/ (mW cm ²)	–	–	[113]
CH ₃ NH ₃ PbI ₃	TENG	UV-visible	7.5 V/W		<80 ms/–	[95]

employed in touch screens and interactive electronics [114]. There are so many novel functional materials including QDs, inorganic nanostructures, 2D layered semiconductors, organic semiconductors, etc., which have been extensively studied as the active layers in flexible optoelectronic devices. Particularly, metal halide perovskites exhibit excellent electrical

and optical properties, as well as outstanding mechanical stability, and they have been used as cost-effective flexible PDs [8,115,116]. For high-sensitivity flexible PDs, both high photoresponsivity and mechanical flexibility should be implemented simultaneously in a single device, which sets a great challenge for fabrication techniques and selection of materials

[117]. High-temperature processing is also another important factor in order to improve the crystallinity of photosensing material in some cases; there are great obstacles to fabricating devices on flexible substrates such as plastic. Cost-effective perovskite material, which exhibits advantages of solution processing and low-temperature fabrication is the promising light-harvesting material for fabrication of high-performance flexible PDs. The majority of flexible devices fabricated to date have been on ITO transparent conducting electrodes and are fabricated by a solution-processing technique at low temperatures, but ITO is also not the best choice owing to its fragility. Therefore, some other alternatives have also been used, such as carbon nanotubes, graphene, metal nanowires, and conducting polymers [118–122]. Overall, flexible PDs must be fabricated at low temperatures and have specific advantages such as a simple processing technique, low cost, shock resistance, light weight, durability, and portability.

Generally, self-powered flexible PDs (SFPDs) are fabricated as two-terminal photodiode structures by utilizing semiconducting junctions (e.g., p-n, p-i-n, Schottky). For example, Cen *et al.* developed an SFPD with a vertical structure with the configuration of FTO/Al₂O₃/CsPbBr₃/TiO₂/Au [123]. The atomic layer deposition (ALD) technique was used to modify the interface of FTO/CsPbBr₃ with Al₂O₃ and Au/CsPbBr₃ with TiO₂ to enhance the charge carrier transport

across the junction [inferred from smooth surface morphology of CsPbBr₃ thin film on Al₂O₃ layer as shown in Fig. 10(a)]. The as-fabricated device shows an enhanced photocurrent [Fig. 10(b)]. Under the dark condition, the ALD – Al₂O₃ layer can act as the electron blocking layer, which accounts for a largely suppressed dark current. Under light conditions, a large number of electrons would be generated in the CsPbBr₃ active layer and also be blocked. Due to the favored energy alignment of ALD – TiO₂ layer (–4.06 eV) between the conduction band of CsPbBr₃ (–3.6 eV) and Au (–5.1 eV), the electrons can be easily transferred to the TiO₂ modification layer. The TiO₂ layer serves as an ETL and contributes to the efficient carrier separation, which can significantly reduce the carrier recombination in the interface of CsPbBr₃/TiO₂ [Fig. 10(c)]. The as-fabricated device shows self-powered functionality at 405 nm wavelength, with high specific detectivity of 1.88×10^{13} Jones, broad LDR of 172.7 dB, low detectible limit of 4.3 nW cm^{-2} , as well as the ultralow dark current of 10^{-11} A [Figs. 10(d) and 10(e)]. Moreover, the device exhibits excellent environmental stability under light illumination, as shown in Fig. 10(f), and the device also retains its photocurrent even after 3000 bending cycles.

Generally, the PDs with an ohmic contact need an external voltage to split electron–hole pairs produced in the photoactive layer under illumination. However, if semiconductors and elec-

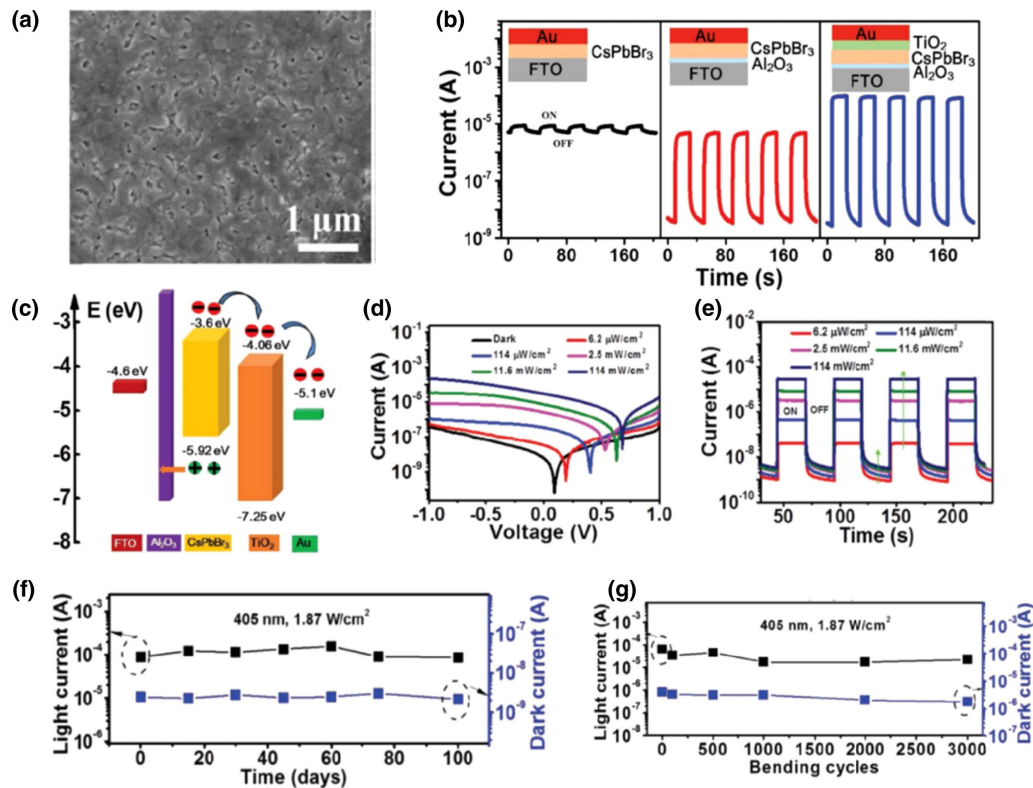


Fig. 10. (a) Plane-view SEM image of CsPbBr₃ perovskite thin films Al₂O₃-modified FTO substrates; (b) photoresponse curves of CsPbBr₃ perovskite PDs, Al₂O₃/CsPbBr₃ perovskite PDs, and Al₂O₃/CsPbBr₃/TiO₂ perovskite PDs, respectively; (c) energy band diagram of hetero-junctions; (d) current–voltage (*I*-*V*) curves of PDs under dark and illumination of 405 nm laser with intensity of $6.2 \mu\text{W cm}^{-2}$ to 114 mW cm^{-2} ; (e) photoresponse curves of ACT PDs under modulated 405 nm laser with various light intensity (0 V); (f) light current and dark current stability at different days for hard substrate device; (g) light current and dark current of flexible device after different bending cycles. Reproduced with permission from Ref. [123]. Copyright 2019, Wiley-VCH.

trodes exhibit asymmetric contact, the PDs with nonsymmetrical Schottky contact can work without an external bias [50]. This is because the Schottky junction promotes photocarrier separation and transport processes in the PDs due to the built-in potential in the junction. Recently, Luo and coworkers reported SFPDs with a metal–semiconductor–metal structure by using MAPbI₃ microwire arrays as a functional layer [Fig. 11(a)], in which asymmetric electrodes were used to produce strong built-in potential [71]. Here, Au/Ag electrodes were chosen to be asymmetric electrode pairs because they exhibit a maximum open-circuit voltage (V_{oc}) of 0.62 V and short-circuit current (I_{sc}) of 0.57 nA, respectively [Figs. 11(b) and 11(c)]. The PD based on Au/Ag electrodes presented a favorable detectivity of 1.3×10^{12} Jones. In addition, the calculated photoresponsivity and response speeds were 161.1 mA W^{-1} and $13.8/16.1 \mu\text{s}$, respectively. Finally, the bending tests demonstrated that the FPDs showed excellent flexibility and mechanical durability, as presented in Fig. 11(d).

In another approach, the appropriate doping of the photoactive layer would enhance the PD performance and ensure flexible compatibility. Toward that direction, Shin *et al.* reported the photodiode structure using graphene QDs (GQDs): CH₃NH₃PbI₃ as the photoactive layer and PEDOT:GQDs as the hole transport layer (HTL) [124]. By incorporating GQDs, along with the increase of perovskite layer crystallinity, the work function of PEDOT: GQD HTL is also increased due to modification of PEDOT from benzodide to quinoid by adding carbon-based material, which leads to the efficient generation of charge carriers and reduced recombination at the interface. The typical device structure and its corresponding cross-sectional scanning electron microscopy (SEM) image are presented in Fig. 11(e). The consecutively enhanced photoresponsivity of 0.354 A W^{-1} and specific detectivity D^* of 8.42×10^{12} Jones were observed, as shown in Fig. 11(f).

Furthermore, the flexible PDs also show excellent stability by maintaining 80% of the initial responsivity even after repeated bending for 1000 cycles at a bending radius of 4 mm [Fig. 11(g)].

Recently, ferroelectric semiconductors have been hybridized with a perovskite photoactive layer for SFPDs by utilizing the concept of polarization by applied potential and generate a built-in electric field to separate the charge carriers, as indicated in Fig. 12(a). For instance, Li *et al.* reported high-performance SFPDs by integrating ferroelectric P(VDF-TrFE) with a perovskite nanowire array heterojunction [125]. The highly flexible device has been fabricated by imprinting technique via DVD-R as master, as shown in Fig. 12(b). Here, polarization was induced by applying +5 V for 5 min; a photoresponsivity R of 12.5 mA W^{-1} , a specific detectivity D^* of 7.3×10^{12} Jones, and a t_{rise}/t_{decay} of $88/154 \mu\text{s}$ under 650 nm light radiation were obtained [Fig. 12(c)]. Moreover, the device shows outstanding stability after several hundreds of bending cycles at different bending angles from 0° to 180° when the intersection angle between bending direction and nanowire direction varies from 0° to 90° [Fig. 12(d)]. The same group demonstrated the bulk heterojunction PD by hybridizing ferroelectric P(VDF-TrFE) with the perovskite layer [126]. The device shows a high level of mechanical stability under multiple bending cycles of 200 [Fig. 12(e)]. So, the results implied that ferroelectric materials can enhance the polarization effect of perovskite, thereby promoting the self-powered performance of PDs. Xiong and coworkers reported a high-performance flexible perovskite PD based on low-cost carbon cloth via an easy solution-processable strategy [127]. The devices exhibited excellent stability in a broadband spectrum (UV to NIR) range. However, the relatively low conductivity of carbon nanotube and PEDOT:PSS limits the performance of the devices. Recently, Shen *et al.* reported SFPD arrays using colloiddally

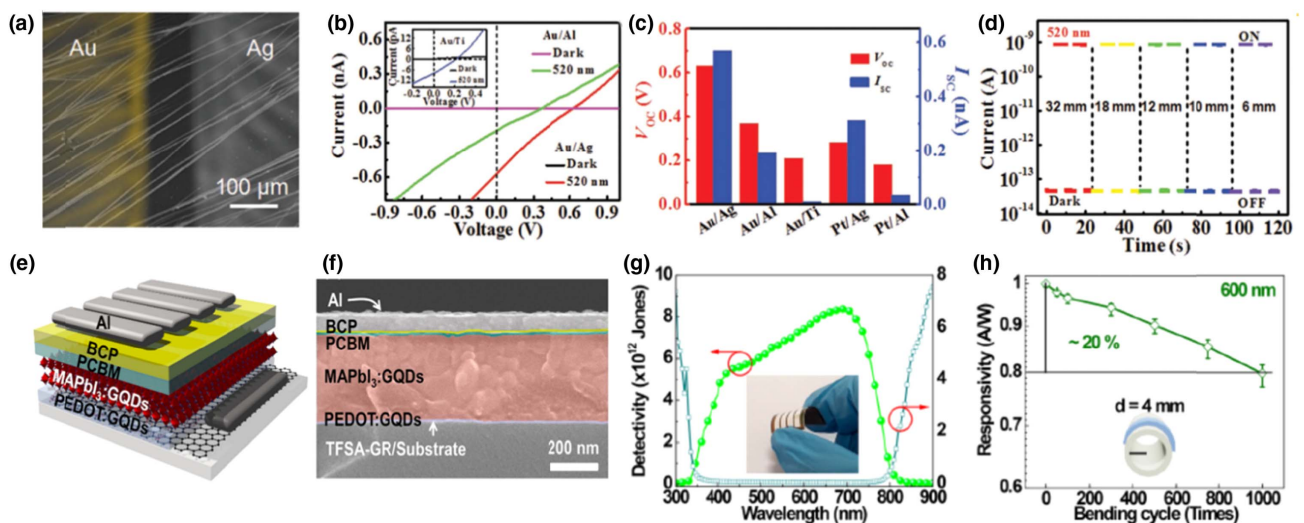


Fig. 11. (a) FESEM image of a typical PD with Au/Ag electrode pair; (b) I - V curves of the CH₃NH₃PbI₃ MWs array-based PDs with asymmetric contact electrodes (Au/Ag, Au/Al); (c) histogram of V_{oc} and I_{sc} for devices with different asymmetric electrode pairs; (d) dark current and photocurrent of the flexible PD being bent to various radii. Reproduced with permission from Ref. [71]. Copyright 2019, Wiley-VCH. (e) Device structure and (f) cross-sectional SEM image of MAPbI₃:graphene QD based PD. (g) NEP/spectral detectivity of PD. The inset shows excellent flexibility of the PD. (h) Evolution of responsivity during repeated 1000 bending cycles at $\lambda = 600 \text{ nm}$ and $d = 4 \text{ mm}$. Reproduced with permission from Ref. [124]. Copyright 2019, American Chemical Society.

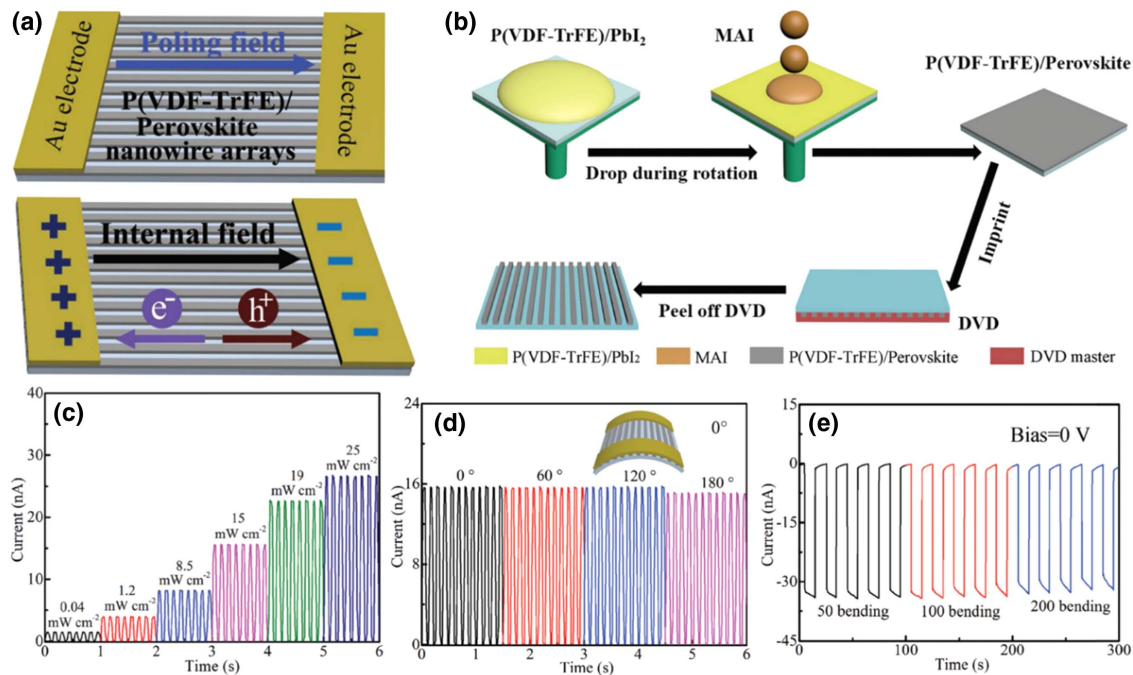


Fig. 12. (a) Schematic illustration of ferroelectric polarization-induced formation of internal electric field in the nanowire array device; (b) schematic illustration of the fabrication process of flexible P(VDF-TrFE)/perovskite hybrid nanowire arrays-based PD; (c) 650 nm wavelength light illumination of flexible P(VDF-TrFE)/perovskite PDs with various power intensities at 0 V; (d) $I-t$ curves of the poled perovskite-0.6 device under 650 nm light illumination at bending angles with the intersection angle between bending direction and nanowire direction of 0° . Reproduced with permission from Ref. [125]. Copyright 2019, Wiley-VCH. (e) $I-t$ curve of flexible P(VDF-TrFE)/perovskite PDs at different bending cycles. Reproduced with permission from Ref. [126]. Copyright 2019, Wiley-VCH.

synthesized CsPbBr₃ QDs on an ITO/PET substrate [128]. The as-fabricated PD arrays show high open-circuit voltage of 1.3 V, photoresponsivity of 10.1 A W^{-1} , and specific detectivity of 9.35×10^{13} Jones.

Apart from the SPPDs based on semiconducting junction properties and (or) inherent materials properties, a highly flexible SFPDs can be achieved by integrating with energy storage units such as solar cells and NGs [129,130]. Given that, Leung *et al.* have designed a novel SFPD that integrates the TENG power source as the hanging unit with a perovskite photoactive layer [129]. The TENG source unit consists of flexible ITO-coated polymer substrate ITO/PET and polydimethylsiloxane (PDMS)/PET separated by a 5 mm gap, as shown in Fig. 13(a). The photoactive perovskite layer was deposited on the PET side of the ITO/PET substrate and impedance matching was provided by a series of resistors. Finally, with the optimized device condition, a photoresponsivity of $79.4 \text{ V mW}^{-1} \text{ cm}^{-2}$ and a specific detectivity of 1.22×10^{13} Jones have been achieved under different detection modes [Fig. 13(b)]. Moreover, as the PD is made of flexible polymer films, it demonstrates no degradation in device performance after being bent 1000 times. Because its polymer base is mostly transparent, the PD also functions at 360° of illumination [Fig. 13(c)]. Besides, the voltage of the device maintained unchanged while being powered by finger tapping 1000 times at various angles of curvature, implying good mechanical endurance.

Instead of mechanically actuated NGs, the in-built solar cell system can also be an excellent choice for SPPDs. For example, an all-perovskite self-powered nanosystem was demonstrated by

Li *et al.*, who assembled the perovskite solar cell with a perovskite PD, as shown in Fig. 13(d) [130]. The authors fabricated planar configuration perovskite solar cell using TiO₂ as an electron transport layer, CH₃NH₃PbI₃ as the light-absorbing layer, and P3HT as the hole transport layer. The as-fabricated solar cell was connected to ITO/CH₃NH₃PbI₃/ITO configured planar PD on a flexible PET substrate through Cu wire, and another side of the PD was connected with the amplifier to measure photocurrent. As an energy conversion unit in the nanosystem, the perovskite solar cell with a high efficiency of 10.5% drives the light-sensing unit to achieve the detection of various lights. Under AM1.5 irradiation (100 mW cm^{-2}), the perovskite solar cell can provide a 0.93 V voltage for the PD [Fig. 13(e)]. Furthermore, the mechanical stability and durability of the PD were examined by multiple bending exercises and no obvious degradation of photoresponse behavior was observed, even after 200 bending cycles, implying good mechanical endurance, as shown in Fig. 13(f).

In addition to the aforementioned SFPD structures, numerous reports have appeared in the literature, as summarized in Table 3. As an example, nanowire array-based PDs show poor photoresponse performance due to the existence of multiple microinterfaces between randomly oriented nanowires, which has been systematically studied by Zeng *et al.* [131]. The authors fabricated nanowire network (NWN) PDs with a welding strategy that showed ultrahigh performance with an on-off ratio and detectivity of 2.8×10^4 and 4.16×10^{13} Jones, respectively. More importantly, the unpackaged NWN PDs show ultrahigh storage stability in the air with a humidity of

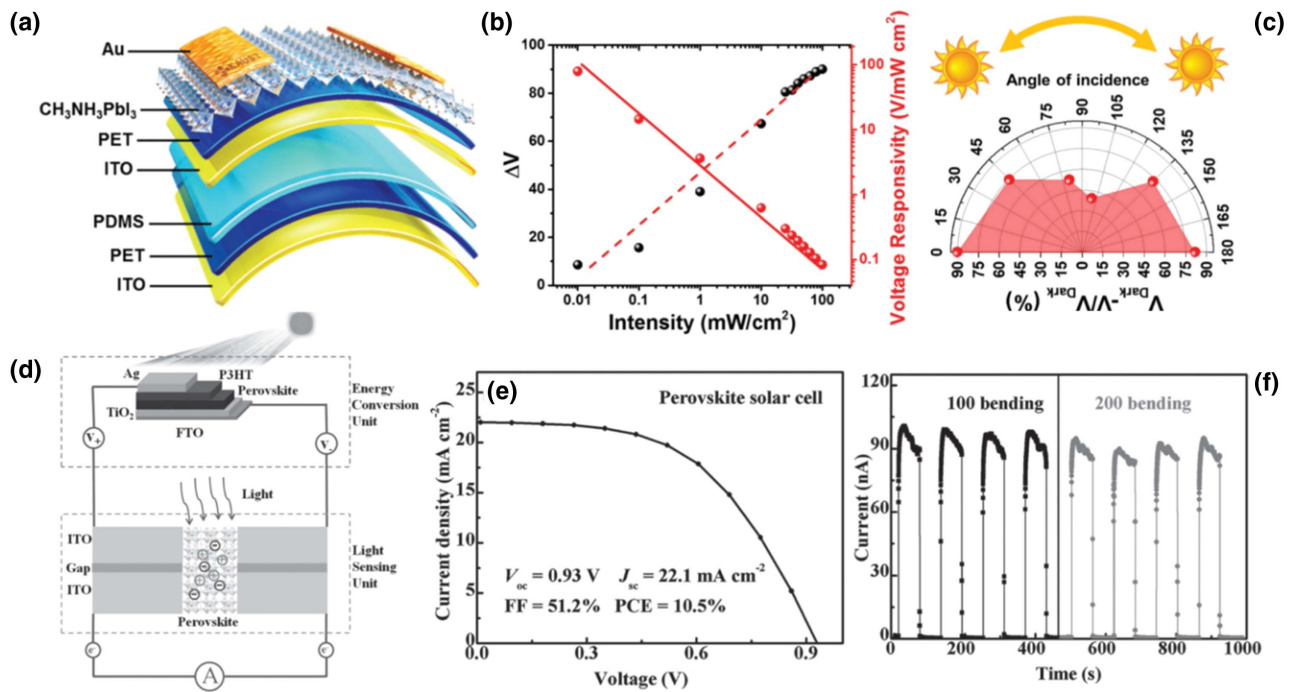


Fig. 13. (a) Schematic diagram of the SFPDs with integrated TENG; (b) change in the measured voltage (ΔV) and voltage responsivity of the device at different light intensities; (c) ΔV at various angles of incident light. Reproduced with permission from Ref. [129]. Copyright 2018, Wiley-VCH. (d) Schematic illustration of the integrated nanosystem, consisting of an energy conversion unit, a light sensing unit, and a current measurement system. (e) J - V curves of the as-fabricated integrated perovskite solar cell; (f) photoresponse curves after 100 and 200 bending cycles. Reproduced with permission from Ref. [130]. Copyright 2016, Wiley-VCH.

Table 3. Summary of Flexible Self-Powered Perovskite-Based PDs

Primary Component of the PD Device Structure	Physical Mechanism for Self-Mode (Junction)	R (mA W^{-1}) (Response Wavelength)	D^* (Jones)	τ_r/τ_f	Bending Cycle	Reference
ITO/ $\text{CH}_3\text{NH}_3\text{PbI}_3$ /Au	Integrated TENG	418 (sunlight)	1.22×10^{13}	80/80 ms	1000	[132]
Au/ $\text{CH}_3\text{NH}_3\text{PbI}_3\text{NRs}$ /Au	PV (Schottky junction)	2.2 (300 nm)	1.76×10^{11}	27.2/26.2 ms	–	[132]
Gr/PEDOT:PSS:GQDs/ $\text{CH}_3\text{NH}_3\text{PbI}_3$:GQDs/PCPM/BCP/Al	PV (heterojunction)	420 (600 nm)	8.42×10^{12}	0.96 μs /–	1000	[127]
Au/ $\text{CH}_3\text{NH}_3\text{PbI}_3$ MWs/Ag	PV (Schottky junction)	161.1 (520 nm)	1.3×10^{12}	13.8/16.1 μs	–	[73]
Ag/Spiro/ $\text{CH}_3\text{NH}_3\text{PbI}_3$ /In ₂ O ₃ /ITO	PV (heterojunction)	451 (720 nm)	1.1×10^{11}	<200/<200 ms	500	[133]
FTO/Al ₂ O ₃ /CsPbBr ₃ /TiO ₂ /Au	PV (heterojunction)	440 (405 nm)	1.88×10^{13}	28/270 μs	3000	[126]
Al/BCP/PCBM/ $\text{CH}_3\text{NH}_3\text{PbI}_3$ /PEDOT:PSS/AuCl ₃ -graphene	PV (heterojunction)	400 (600 nm)	5.3×10^{13}	–	1000	[134]
Au/PTAA/MAPI ₃ /ZnO/n-type GR	PV (heterojunction)	343 (700 nm)	5.82×10^9	1/1 μs	1000	[135]
C/TiO ₂ /perovskite/CuO/Cu ₂ O/Cu	PV (heterojunction)	563 (800 nm)	2.15×10^{13}	<200/<200 ms	60	[136]
ITO/ $\text{CH}_3\text{NH}_3\text{PbI}_3$ /ITO	Solar cell	110 (730 nm)	–	2200/300 ms	200	[133]
Au/P(VDF-rFE)/ $\text{CH}_3\text{NH}_3\text{PbI}_3$ /Au	PV (heterojunction)	20 (650 nm)	1.4×10^{13}	92/193 μs	200	[129]
Au/P(VDF-TrFE)/ $\text{CH}_3\text{NH}_3\text{PbI}_3$ nanowires/Au	PV (heterojunction)	12 (650 nm)	7.3×10^{12}	88/184 μs	200	[128]
Au NWs/PEDOT:PSS/ $\text{CH}_3\text{NH}_3\text{PbI}_3$ /PCPM/Al	PV (heterojunction)	321 (670 nm)	–	4/3.3 μs	–	[123]
C/TiO ₂ /perovskite/SpiroOMeTAD/Au	PV (heterojunction)	182 (750 nm)	1.24×10^{11}	<200/<200 ms	80	[130]
Ni/ $\text{CH}_3\text{NH}_3\text{PbI}_3$ /Al	PV (Schottky junction)	227 (532 nm)	1.36×10^{11}	61/42 ms	1500	[72]
ITO/TiO ₂ /CsPbBr ₃ /SpiroOMeTAD/Au	PV (heterojunction)	10.1×10^3 (405 nm)	9.35×10^{13}	8.0/2.3 s	1600	[136]

55%–65%, and the flexible NWN PDs can withstand 250 bending cycles at different bending radii and 1000 bending cycles at fixed bending radii with no performance degradation being observed. Also, a self-powered flexible fiber-shaped PD based on double-twisted perovskite-TiO₂-carbon fiber and CuO-Cu₂O-Cu wire was designed by Li *et al.* and achieved an ultrahigh detectivity of 2.15×10^{13} Jones and response time of less than 200 ms [136]. Recently, Ogale *et al.* demonstrated the flexible self-powered PD by forming a heterojunction of SnO₃ and cubic phase α -CsPbI₃ [101]. The cubic phase of CsPbI₃ was stabilized by polyvinylpyrrolidone (PVP) wrapping, by which the device performance and environmental stability of the device have been notably enhanced.

7. CHALLENGES AND FUTURE PERSPECTIVE

The perovskite-based SPPD operable at various subbands from DUV to the NIR has been achieved. However, the significant advantages and disadvantages regarding perovskite-based PDs are applicable to perovskite-based self-powered PDs too. Despite significant development in perovskite PDs, there are still formidable issues and challenges to be resolved to shift from laboratory to industrial mass production and application. The performance can be further improved by optimizing the intrinsic properties of perovskite material and device fabrication schemes. Apart from key parameters such as photosensitivity, photoresponsivity, detectivity, and response speed, the important criteria for practical device application are that the device has to maintain a stable photocurrent and dark current for the long term under standard conditions. This criterion has mainly been affected by issues such as moisture, thermal condition, and photoinstability [137,138].

A. Stability against Moisture

Mostly, perovskite-based optoelectronic devices are based on hybrid organic-inorganic perovskite materials, which have non-coordinated ions such as Pb²⁺, I⁻, and MA⁺ that were responsible for the perovskites to be highly sensitive to moisture and polar solvent and subsequently affect the stability of the perovskite [139,140]. It was found that large-sized cations (i.e., long-chain organic cations) can enhance the stability of perovskite materials [89,141]. The perovskite materials with long-chain cations showed negligible degradation after exposure to moisture for 46 days. It was also reported that the Pb-containing perovskites are stabler in air than their Sn-containing counterparts because Sn²⁺ is easy to be oxidized to Sn⁴⁺. Specifically, the Pb-containing perovskites show only surface degradation in the dark with the bulk properties of the materials retained for a couple of weeks in air. Moreover, it was observed that the metal luster in MAPbI₃ single crystals can even keep for more than half a year in air. In contrast, the Sn-containing materials are air- and moisture-sensitive and partially decompose within 2 h before total decomposition after 1 day [142]. Apart from the crystal structure of perovskite, the defect structure of perovskites plays an important role in the deterioration of device performance [143]. The presence of defects in light-sensitive material has commonly been recognized as fatal, such that charge mobility, carrier lifetime, and conductivity are decreased, which are inevitable properties

for optoelectronic devices. A stability study on polycrystalline thin film performed by Wang *et al.* reported that deterioration of perovskite occurs due to the large number of grain boundaries and surface defects. On the other hand, single-crystal perovskites with no grain boundary and diminished surface defects show better stability in the air for a longer time [144]. It has been concluded that the hybrid perovskites tend to decompose due to the hygroscopic nature of amine salts, and degeneration mainly starts at the structural defects of crystal as well as at grain boundaries [145].

B. Stability against Temperature

Besides the moisture, the device performance is also highly affected by temperature gradient. At different operating temperatures, perovskite material can undergo phase transitions. These dissimilar thermally induced phases of the perovskite acquire unique optical and carrier transport properties. This dissimilarity in the properties creates a chief problem for potential implementation of perovskite devices [146]. Bao *et al.* carried out the thermal stability test of CsPbI₃, CsPbBr₃, and MAPbI₃ perovskite-based PDs, as shown in Fig. 14(a) [88]. It was found that the photoresponsivity of MAPbI₃ devices experienced a fast decay to 80% of its initial value within 24 h, and then degraded quickly to almost zero within 125 h. In contrast, after about 244 h of heating, the photoresponsivity of CsPbBr₃ devices does not show any obvious degradation, and that of CsPbI₃ devices degrades about 40%, which can be contributed to contact corrosion due to the reaction between I in the perovskite active layer and the Ag electrodes under high temperature. The decomposition of MAPbI₃ under thermal treatment is clearly illustrated by the X-ray diffraction (XRD) study of devices, as presented in Figs. 14(b) and 14(c). Gui *et al.* demonstrated the thermal stability of a device made up of CsPbBr_{3-x}Cl_x microplatelets, where the device can withstand temperatures up to 250°C [75]. Chandrasekar *et al.* studied the influence of thermal treatment on MAPbI₃ nanocrystal thin film, as shown in Fig. 14(d) and drew the inference that MAPbI₃ CQDs thin films can withstand temperatures up to 50°C [50]. In addition to material stability under temperature, the PD performance under thermal treatment was studied in single-crystal MAPbI₃ by Zhang *et al.* [60]. It was found that decrement of photocurrent observed with an increment of temperature up to 60°C can be ascribed to the decrease of polarization strength as the temperature increases.

C. Stability against Light Exposure

Perovskite semiconductors demand deep investigation with respect to their stability in terms of moisture and temperature. However, the encapsulation technique could give the solution to enhance the stability to some extent. Stability under light exposure is another challenge to be faced while dealing with perovskite-based PDs [137]. The deep insight into the mechanism of light-induced degradation will be valuable for designing highly stable perovskite materials [147]. There are many reports on the degradation of perovskites under light illumination. The hypotheses include electronic trap states [148], photochemical reactions [149,150], activate transport of halide ions and/or organic cations [151], etc. Bag *et al.* studied the stability of perovskite under light exposure by replacing an MA⁺

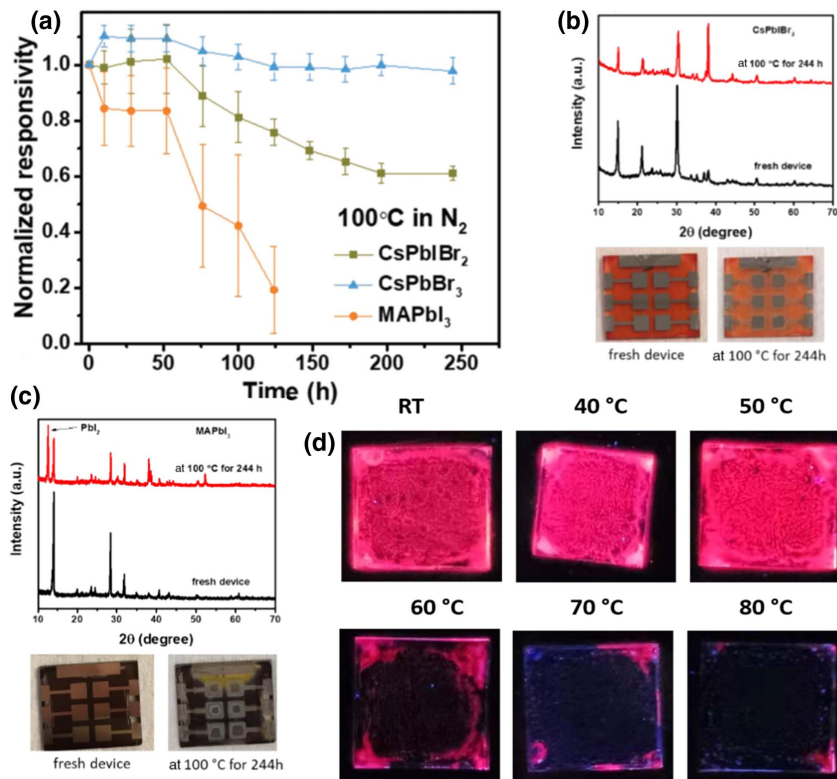


Fig. 14. (a) Photoresponsivity evolution of PDs based on inorganic perovskite $\text{CsPbI}_x\text{Br}_{3-x}$ and hybrid perovskite MAPbI_3 at 100°C in N_2 ambient condition. XRD spectra and digital photographs of (b) $\text{CsPbI}_2\text{Br}_2$ and (c) MAPbI_3 devices before and after heated at 100°C in N_2 -filled glove box for 244 h. The obvious PbI_2 peak in XRD spectrum of MAPbI_3 devices after being heated indicates the decomposition of MAPbI_3 . Reproduced with permission from Ref. [88]. Copyright 2018, Wiley-VCH. (d) Thermal stability of MAPbI_3 NCs; photographic image of samples under 365 nm illumination. The samples are annealed at 40°C , 50°C , 60°C , 70°C , and 80°C for 10 min in open air. Reproduced with permission from Ref. [50]. Copyright 2020, Wiley-VCH.

(methylammonium) ion with an FA^+ (formamidinium) ion; stability was enhanced by optimizing the balance between MA^+ and FA^+ ions [151]. Hence, it can be concluded that the controlling of vacancy defects and ion migration deficiency can considerably enhance the stability of perovskite-based devices under long-term exposure to light illumination.

D. Issue of Toxicity

Several issues and open questions regarding the commercialization of perovskite-based PDs remain to be confronted. The toxicity caused by lead is always a problem, threatening human health, poisoning organisms, polluting the environment, and causing difficulty in discharging lead from the body. Research indicates that the contamination of lead ions to soil and water sources is permanent and generates a very serious negative impact on human, animal, and plant survival [152–155]. Therefore, to assure human safety and a pollution-free natural environment, it is very essential to develop some non- or low-toxic metal ions to replace lead as perovskite materials. For example, there have been multiple previous attempts to replace Pb^{2+} ions by less toxic ions such as Sn^{2+} , Bi^{3+} , Ge^{2+} , Sb^{3+} , Mn^{2+} , and Cu^{2+} ions [156–160]. These efforts not only increase the variety of perovskite materials but also enhance the environmentally friendly features. Although the toxicity has been weakened by lead-free perov-

skites, the performance of the device needs to be further improved. Among the perovskite components, lead acts as a core skeleton that plays an important role in the generation and transport of charges. The carriers transfer along with the Pb–halogen bond, resulting in poor performance and lower stability after replacing Pb with Sn or Bi. Many researchers have proved that the role of lead is irreplaceable; thus the toxicity treatment of perovskite needs to be further considered. Overall, to facilitate a profound understanding of perovskite characteristics and device physics, the focus should be sharpened to their crystal growth process, defect engineering, device fabrication technique, and more importantly, the stability of devices under ambient conditions.

8. CONCLUSION

In summary, by virtue of their superior optoelectronic properties, perovskite materials have made a giant step in the PDs research field. Although significant advances in the development of perovskite-based self-powered PDs have been made in past years, there are still some challenges remaining before moving forward with practical applications. There are two ways to bring the perovskite-based PDs to practical or commercial application: either by optimization of material synthesis with high crystal quality and enhancement of stability issues in

perovskite material or advancement in device fabrication strategy. Moreover, PD arrays are less explored for real applications in imaging and biomedical sensing, which should be a focus in the future. Specifically, the fabricated self-powered perovskite PDs should be intelligent, multifunctional, supersmall, extremely sensitive, and energy-efficient. This requires the rational synthesis of materials, fabrication of devices, and integration of various devices into a system with multifunctional characteristics and operation without external power sources. We strongly believe that the reader can acquire more comprehensive knowledge in this field while reading this review and motivate young researchers to undertake the tasks to solve the issues raised in this review.

Funding. National Key Research and Development Program of China (2018YFB2200500); National Natural Science Foundation of China (61974170, 61934007); Beijing Municipal Science and Technology Commission (Z191100004819011); International Collaboration Project of Ministry of Science and Technology (DL20200001030).

Disclosures. The authors declare no conflicts of interest.

REFERENCES

- J. Yu, G. Liu, C. Chen, Y. Li, M. Xu, T. Wang, G. Zhao, and L. Zhang, "Perovskite CsPbBr₃ crystals: growth and applications," *J. Mater. Chem. C* **8**, 6326–6341 (2020).
- B. Murali, H. K. Kolli, J. Yin, R. Ketavath, O. M. Bakr, and O. F. Mohammed, "Single crystals: the next big wave of perovskite optoelectronics," *ACS Mater. Lett.* **2**, 184–214 (2020).
- F. Mei, D. Sun, S. Mei, J. Feng, Y. Zhou, J. Xu, and X. Xiao, "Recent progress in perovskite-based photodetectors: the design of materials and structures," *Adv. Phys. X* **4**, 1592709 (2019).
- H. Wang and D. H. Kim, "Perovskite-based photodetectors: materials and devices," *Chem. Soc. Rev.* **46**, 5204–5236 (2017).
- B. Saparov and D. B. Mitzi, "Organic-inorganic perovskites: structural versatility for functional materials design," *Chem. Rev.* **116**, 4558–4596 (2016).
- M. A. Green, A. Ho-Baillie, and H. J. Snaith, "The emergence of perovskite solar cells," *Nat. Photonics* **8**, 506–514 (2014).
- G. Konstantatos and E. H. Sargent, "Nanostructured materials for photon detection," *Nat. Nanotechnol.* **5**, 391–400 (2010).
- F. H. L. Koppens, T. Mueller, P. Avouris, A. C. Ferrari, M. S. Vitiello, and M. Polini, "Photodetectors based on graphene, other two-dimensional materials and hybrid systems," *Nat. Nanotechnol.* **9**, 780–793 (2014).
- Z. L. Wang, "Self-powered nanosensors and nanosystems," *Adv. Mater.* **24**, 280–285 (2012).
- J. Gubbi, R. Buyya, S. Marusic, and M. Palaniswami, "Internet of things (IoT): a vision, architectural elements, and future directions," *Future Gener. Comput. Syst.* **29**, 1645–1660 (2013).
- Y. Yang, W. Guo, J. Qi, J. Zhao, and Y. Zhang, "Self-powered ultraviolet photodetector based on a single Sb-doped ZnO nanobelt," *Appl. Phys. Lett.* **97**, 223113 (2010).
- Y.-Q. Bie, Z.-M. Liao, H.-Z. Zhang, G.-R. Li, Y. Ye, Y. B. Zhou, J. Xu, Z.-X. Qin, L. Dai, and D.-P. Yu, "Self-powered, ultrafast, visible-blind UV detection and optical logical operation based on ZnO/GaN nanoscale p-n junctions," *Adv. Mater.* **23**, 649–653 (2011).
- X. Li, L. Tao, Z. Chen, H. Fang, X. Li, X. Wang, J.-B. Xu, and H. Zhu, "Graphene and related two-dimensional materials: structure-property relationships for electronics and optoelectronics," *Appl. Phys. Rev.* **4**, 021306 (2017).
- C. Li, Q. Cao, F. Wang, Y. Xiao, Y. Li, J.-J. Delaunay, and H. Zhu, "Engineering graphene and TMDs based van der Waals heterostructures for photovoltaic and photoelectrochemical solar energy conversion," *Chem. Soc. Rev.* **47**, 4981–5037 (2018).
- M. Dai, H. Chen, R. Feng, W. Feng, Y. Hu, H. Yang, G. Liu, X. Chen, J. Zhang, C.-Y. Xu, and P. Hu, "A dual-band multilayer InSe self-powered photodetector with high performance induced by surface plasmon resonance and asymmetric Schottky junction," *ACS Nano* **12**, 8739–8747 (2018).
- X. Zhou, X. Hu, J. Yu, S. Liu, Z. Shu, Q. Zhang, H. Li, Y. Ma, H. Xu, and T. Zhai, "2D layered material-based van der Waals heterostructures for optoelectronics," *Adv. Funct. Mater.* **28**, 1706587 (2018).
- J. Miao and F. Zhang, "Recent progress on highly sensitive perovskite photodetectors," *J. Mater. Chem. C* **7**, 1741–1791 (2019).
- L. Su, W. Yang, J. Cai, H. Chen, and X. Fang, "Self-powered ultraviolet photodetectors driven by built-in electric field," *Small* **13**, 1701687 (2017).
- W. Tian, Y. Wang, L. Chen, and L. Li, "Self-powered nanoscale photodetectors," *Small* **13**, 1701848 (2017).
- M. Liu, M. B. Johnston, and H. J. Snaith, "Efficient planar heterojunction perovskite solar cells by vapour deposition," *Nature* **501**, 395–398 (2013).
- J. Huang, Y. Yuan, Y. Shao, and Y. Yan, "Understanding the physical properties of hybrid perovskites for photovoltaic applications," *Nat. Rev. Mater.* **2**, 17042 (2017).
- L. Etgar, P. Gao, Z. Xue, Q. Peng, A. K. Chandiran, B. Liu, M. K. Nazeeruddin, and M. Grätzel, "Mesoscopic CH₃NH₃PbI₃/TiO₂ heterojunction solar cells," *J. Am. Chem. Soc.* **134**, 17396–17399 (2012).
- A. Miyata, A. Mitioglu, P. Plochocka, O. Portugall, J. T.-W. Wang, S. D. Stranks, H. J. Snaith, and R. J. Nicholas, "Direct measurement of the exciton binding energy and effective masses for charge carriers in organic-inorganic tri-halide perovskites," *Nat. Phys.* **11**, 582–587 (2015).
- S. Torabi, F. Jahani, V. I. Severen, C. Kanimozhi, S. Patil, R. W. A. Havenith, R. C. Chiechi, L. Lutsen, D. J. M. Vanderzande, T. J. Cleij, J. C. Hummelen, and J. A. Koster, "Strategy for enhancing the dielectric constant of organic semiconductors without sacrificing charge carrier mobility and solubility," *Adv. Funct. Mater.* **25**, 150–157 (2015).
- T. M. Brenner, D. A. Egger, L. Kronik, G. Hodes, and D. Cahen, "Hybrid organic-inorganic perovskites: low-cost semiconductors with intriguing charge-transport properties," *Nat. Rev. Mater.* **1**, 15007 (2016).
- D. Shi, V. Adinolfi, R. Comin, M. Yuan, E. Alarousu, A. Buin, Y. Chen, S. Hoogland, A. Rothenberger, K. Katsiev, Y. Losovyj, X. Zhang, P. A. Dowben, O. F. Mohammed, E. H. Sargent, and O. M. Bakr, "Low trap-state density and long carrier diffusion in organolead trihalide perovskite single crystals," *Science* **347**, 519–522 (2015).
- G. R. Yettapu, D. Talukdar, S. Sarkar, A. Swarnkar, A. Nag, P. Ghosh, and P. Mandal, "Terahertz conductivity within colloidal CsPbBr₃ perovskite nanocrystals: remarkably high carrier mobilities and large diffusion lengths," *Nano Lett.* **16**, 4838–4848 (2016).
- M. I. Saidaminov, M. A. Haque, J. Almutlaq, S. Sarmah, X.-H. Miao, R. Begum, A. A. Zhumekenov, I. Dursun, N. Cho, B. Murali, O. F. Mohammed, T. Wu, and O. M. Bakr, "Inorganic lead halide perovskite single crystals: phase-selective low-temperature growth, carrier transport properties, and self-powered photodetection," *Adv. Opt. Mater.* **5**, 1600704 (2017).
- Y. He, L. Matei, H. J. Jung, K. M. McCall, M. Chen, C. C. Stoumpos, Z. Liu, J. A. Peters, D. Y. Chung, B. W. Wessels, M. R. Wasielewski, V. P. Dravid, A. Burger, and M. G. Kanatzidis, "High spectral resolution of gamma-rays at room temperature by perovskite CsPbBr₃ single crystals," *Nat. Commun.* **9**, 1609 (2018).
- A. Fakhruddin, L. Schmidt-Mende, G. Garcia-Belmonte, R. Jose, and I. Mora-Sero, "Interfaces in perovskite solar cells," *Adv. Energy Mater.* **7**, 1700623 (2017).
- T. Leijtens, G. E. Eperon, N. K. Noel, S. N. Habisreutinger, A. Petrozza, and H. J. Snaith, "Stability of metal halide perovskite solar cells," *Adv. Energy Mater.* **5**, 1500963 (2015).
- A. K. Jena, A. Kulkarni, and T. Miyasaka, "Halide perovskite photovoltaics: background, status, and future prospects," *Chem. Rev.* **119**, 3036–3103 (2019).

33. Y. Zhou and Y. Zhao, "Chemical stability and instability of inorganic halide perovskites," *Energy Environ. Sci.* **12**, 1495–1511 (2019).
34. Y. Lin, Y. Bai, Y. Fang, Q. Wang, Y. Deng, and J. Huang, "Suppressed ion migration in low-dimensional perovskites," *ACS Energy Lett.* **2**, 1571–1572 (2017).
35. H. J. Snaith, A. Abate, J. M. Ball, G. E. Eperon, T. Leijtens, N. K. Noel, S. D. Stranks, J. T.-W. Wang, K. Wojciechowski, and W. Zhang, "Anomalous hysteresis in perovskite solar cells," *J. Phys. Chem. Lett.* **5**, 1511–1515 (2014).
36. A. Fakharuddin, U. Shabbir, W. Qiu, T. Iqbal, M. Sultan, P. Heremans, and L. Schmidt-Mende, "Inorganic and layered perovskites for optoelectronic devices," *Adv. Mater.* **31**, 1807095 (2019).
37. M. Saliba, T. Matsui, J.-Y. Seo, K. Domanski, J.-P. Correa-Baena, M. K. Nazeeruddin, S. M. Zakeeruddin, W. Tress, A. Abate, A. Hagfeldt, and M. Grätzel, "Cesium-containing triple cation perovskite solar cells: improved stability, reproducibility and high efficiency," *Energy Environ. Sci.* **9**, 1989–1997 (2016).
38. J.-W. Lee, D.-H. Kim, H.-S. Kim, S.-W. Seo, S. M. Cho, and N.-G. Park, "Formamidine and cesium hybridization for photo- and moisture-stable perovskite solar cell," *Adv. Energy Mater.* **5**, 1501310 (2015).
39. F. Zhuge, Z. Zheng, P. Luo, L. Lv, Y. Huang, H. Li, and T. Zhai, "Nanostructured materials and architectures for advanced infrared photodetection," *Adv. Mater. Technol.* **2**, 1700005 (2017).
40. Z. Bai, X. Chen, X. Yan, X. Zheng, Z. Kang, and Y. Zhang, "Self-powered ultraviolet photodetectors based on selectively grown ZnO nanowire arrays with thermal tuning performance," *Phys. Chem. Chem. Phys.* **16**, 9525–9529 (2014).
41. X. Chen, K. Liu, Z. Zhang, C. Wang, B. Li, H. Zhao, D. Zhao, and D. Shen, "Self-powered solar-blind photodetector with fast response based on Au/ β -Ga₂O₃ nanowires array film Schottky junction," *ACS Appl. Mater. Interfaces* **8**, 4185–4191 (2016).
42. L. Duan, F. He, Y. Tian, B. Sun, J. Fan, X. Yu, L. Ni, Y. Zhang, Y. Chen, and W. Zhang, "Fabrication of self-powered fast-response ultraviolet photodetectors based on graphene/ZnO:Al nanorod-array-film structure with stable Schottky barrier," *ACS Appl. Mater. Interfaces* **9**, 8161–8168 (2017).
43. M. Hussain, S. Aftab, S. H. A. Jaffery, A. Ali, S. Hussain, D. N. Cong, R. Akhtar, Y. Seo, J. Eom, P. Gautam, H. Noh, and J. Jung, "Asymmetric electrode incorporated 2D GeSe for self-biased and efficient photodetection," *Sci. Rep.* **10**, 9374 (2020).
44. L. Mi, H. Wang, Y. Zhang, X. Yao, Y. Chang, G. Li, G. Li, and Y. Jiang, "High performance visible–near-infrared PbS-quantum-dots/indium Schottky diodes for photodetectors," *Nanotechnology* **28**, 055202 (2016).
45. D. Wu, Y. Jiang, Y. Zhang, Y. Yu, Z. Zhu, X. Lan, F. Li, C. Wu, L. Wang, and L. Luo, "Self-powered and fast-speed photodetectors based on CdS:Ga nanoribbon/Au Schottky diodes," *J. Mater. Chem.* **22**, 23272–23276 (2012).
46. D. Li, G. Dong, W. Li, and L. Wang, "High performance organic-inorganic perovskite-optocoupler based on low-voltage and fast response perovskite compound photodetector," *Sci. Rep.* **5**, 7902 (2015).
47. P. V. Chandrasekar, S. Yang, J. Hu, M. Sulaman, M. I. Saleem, Y. Tang, Y. Jiang, and B. Zou, "A one-step method to synthesize CH₃NH₃PbI₃:MoS₂ nanohybrids for high-performance solution-processed photodetectors in the visible region," *Nanotechnology* **30**, 085707 (2019).
48. R. Zhi, J. Hu, S. Yang, C. Perumal Veeramalai, Z. Zhang, M. I. Saleem, M. Sulaman, Y. Tang, and B. Zou, "A facile method to synthesize two-dimensional CsPb₂Br₃ nano-/micro-sheets for high-performance solution-processed photodetectors," *J. Alloys. Compd.* **824**, 153970 (2020).
49. C. Perumal Veeramalai, S. Yang, R. Zhi, M. Sulaman, M. I. Saleem, Y. Cui, Y. Tang, Y. Jiang, L. Tang, and B. Zou, "Solution-processed," *Adv. Opt. Mater.* **8**, 2000215 (2020).
50. L. Peng, L. Hu, and X. Fang, "Energy harvesting for nanostructured self-powered photodetectors," *Adv. Funct. Mater.* **24**, 2591–2610 (2014).
51. Z. L. Wang, "The new field of photopiezotronics," *Mater. Today* **10**, 20–28 (2007).
52. G. Maculan, A. D. Sheikh, A. L. Abdelhady, M. I. Saidaminov, M. A. Haque, B. Murali, E. Alarousu, O. F. Mohammed, T. Wu, and O. M. Bakr, "CH₃NH₃PbCl₃ single crystals: inverse temperature crystallization and visible-blind UV-photodetector," *J. Phys. Chem. Lett.* **6**, 3781–3786 (2015).
53. Q. Dong, Y. Fang, Y. Shao, P. Mulligan, J. Qiu, L. Cao, and J. Huang, "Electron-hole diffusion lengths >175 μ m in solution-grown CH₃NH₃PbI₃ single crystals," *Science* **347**, 967–970 (2015).
54. Z. Lian, Q. Yan, Q. Lv, Y. Wang, L. Liu, L. Zhang, S. Pan, Q. Li, L. Wang, and J.-L. Sun, "High-performance planar-type photodetector on (100) facet of MAPbI₃ single crystal," *Sci. Rep.* **5**, 16563 (2015).
55. J. Shamsi, A. L. Abdelhady, S. Accornero, M. Arciniegas, L. Goldoni, A. R. S. Kandada, A. Petrozza, and L. Manna, "N-methylformamide as a source of methylammonium ions in the synthesis of lead halide perovskite nanocrystals and bulk crystals," *ACS Energy Lett.* **1**, 1042–1048 (2016).
56. M. Cao, J. Tian, Z. Cai, L. Peng, L. Yang, and D. Wei, "Perovskite heterojunction based on CH₃NH₃PbBr₃ single crystal for high-sensitive self-powered photodetector," *Appl. Phys. Lett.* **109**, 233303 (2016).
57. X. Zhang, C. Ji, X. Liu, S. Wang, L. Li, Y. Peng, Y. Yao, M. Hong, and J. Luo, "Solution-grown large-sized single-crystalline 2D/3D perovskite heterostructure for self-powered photodetection," *Adv. Opt. Mater.* **8**, 2000311 (2020).
58. J. Ding, H. Fang, Z. Lian, J. Li, Q. Lv, L. Wang, J.-L. Sun, and Q. Yan, "A self-powered photodetector based on a CH₃NH₃PbI₃ single crystal with asymmetric electrodes," *CrystEngComm* **18**, 4405–4411 (2016).
59. P. A. Shaikh, D. Shi, J. R. D. Retamal, A. D. Sheikh, M. A. Haque, C.-F. Kang, J.-H. He, O. M. Bakr, and T. Wu, "Schottky junctions on perovskite single crystals: light-modulated dielectric constant and self-biased photodetection," *J. Mater. Chem. C* **4**, 8304–8312 (2016).
60. X. Zhang, X. Dong, S. Wang, H. Liu, W. Hu, and X. Li, "A self-powered photodetector based on polarization-driven in CH₃NH₃PbI₃ single crystal (100) plane," *Chem. Eng. J.* **404**, 125957 (2020).
61. R. Yan, D. Gargas, and P. Yang, "Nanowire photonics," *Nat. Photonics* **3**, 569–576 (2009).
62. Y. Fu, H. Zhu, J. Chen, M. P. Hautzinger, X. Y. Zhu, and S. Jin, "Metal halide perovskite nanostructures for optoelectronic applications and the study of physical properties," *Nat. Rev. Mater.* **4**, 169–188 (2019).
63. D. Chen and X. Chen, "Luminescent perovskite quantum dots: synthesis, microstructures, optical properties and applications," *J. Mater. Chem. C* **7**, 1413–1446 (2019).
64. F. Zhang, H. Zhong, C. Chen, X.-G. Wu, X. Hu, H. Huang, J. Han, B. Zou, and Y. Dong, "Brightly luminescent and color-tunable colloidal CH₃NH₃PbX₃ (X = Br, I, Cl) quantum dots: potential alternatives for display technology," *ACS Nano* **9**, 4533–4542 (2015).
65. L. Protesescu, S. Yakunin, M. I. Bodnarchuk, F. Krieg, R. Caputo, C. H. Hendon, R. X. Yang, A. Walsh, and M. V. Kovalenko, "Nanocrystals of cesium lead halide perovskites (CsPbX₃, X = Cl, Br, and I): novel optoelectronic materials showing bright emission with wide color gamut," *Nano Lett.* **15**, 3692–3696 (2015).
66. Y. Wang, L. Song, Y. Chen, and W. Huang, "Emerging new-generation photodetectors based on low-dimensional halide perovskites," *ACS Photon.* **7**, 10–28 (2020).
67. M. S. Imran, Y. Shengyi, Z. Ruonan, L. Hailong, S. Muhammad, V. PerumalChandrasekar, Z. Zhenheng, B. Attia, and Z. Bingsuo, "Self-powered, all-solution processed, trilayer heterojunction perovskite-based photodetectors," *Nanotechnology* **31**, 254001 (2020).
68. H. Zhou, Z. Song, C. R. Grice, C. Chen, J. Zhang, Y. Zhu, R. Liu, H. Wang, and Y. Yan, "Self-powered CsPbBr₃ nanowire photodetector with a vertical structure," *Nano Energy* **53**, 880–886 (2018).
69. F. Cao, W. Tian, K. Deng, M. Wang, and L. Li, "Self-powered UV–Vis–NIR photodetector based on conjugated-polymer/CsPbBr₃ nanowire array," *Adv. Funct. Mater.* **29**, 1906756 (2019).
70. J. Tao, Z. Xiao, J. Wang, C. Li, X. Sun, F. Li, X. Zou, G. Liao, and Z. Zou, "A self-powered, flexible photodetector based on perovskite nanowires with Ni-Al electrodes," *J. Alloys. Compd.* **845**, 155311 (2020).
71. C.-Y. Wu, W. Peng, T. Fang, B. Wang, C. Xie, L. Wang, W.-H. Yang, and L.-B. Luo, "Asymmetric contact-induced self-driven

- perovskite-microwire-array photodetectors," *Adv. Electron. Mater.* **5**, 1900135 (2019).
72. P. V. Chandrasekar, S. Yang, J. Hu, M. Sulaman, Y. Shi, M. I. Saleem, Y. Tang, Y. Jiang, and B. Zou, "Solution-phase, template-free synthesis of PbI_2 and MAPbI_3 nano/microtubes for high-sensitivity photodetectors," *Nanoscale* **11**, 5188–5196 (2019).
 73. Y. Liu, F. Li, C. Perumal Veeramalai, W. Chen, T. Guo, C. Wu, and T. W. Kim, "Inkjet-printed photodetector arrays based on hybrid perovskite $\text{CH}_3\text{NH}_3\text{PbI}_3$ microwires," *ACS Appl. Mater. Interfaces* **9**, 11662–11668 (2017).
 74. Q. Ou, Y. Zhang, Z. Wang, J. A. Yuwono, R. Wang, Z. Dai, W. Li, C. Zheng, Z.-Q. Xu, X. Qi, S. Duhm, N. V. Medhekar, H. Zhang, and Q. Bao, "Strong depletion in hybrid perovskite p–n junctions induced by local electronic doping," *Adv. Mater.* **30**, 1705792 (2018).
 75. P. Gui, J. Li, X. Zheng, H. Wang, F. Yao, X. Hu, Y. Liu, and G. Fang, "Self-driven all-inorganic perovskite microplatelet vertical Schottky junction photodetectors with a tunable spectral response," *J. Mater. Chem. C* **8**, 6804–6812 (2020).
 76. C. Tian, F. Wang, Y. Wang, Z. Yang, X. Chen, J. Mei, H. Liu, and D. Zhao, "Chemical vapor deposition method grown all-inorganic perovskite microcrystals for self-powered photodetectors," *ACS Appl. Mater. Interfaces* **11**, 15804–15812 (2019).
 77. H. Zhou, J. Zeng, Z. Song, C. R. Grice, C. Chen, Z. Song, D. Zhao, H. Wang, and Y. Yan, "Self-powered all-inorganic perovskite microcrystal photodetectors with high detectivity," *J. Phys. Chem. Lett.* **9**, 2043–2048 (2018).
 78. H. Zhou, Z. Song, C. R. Grice, C. Chen, X. Yang, H. Wang, and Y. Yan, "Pressure-assisted annealing strategy for high-performance self-powered all-inorganic perovskite microcrystal photodetectors," *J. Phys. Chem. Lett.* **9**, 4714–4719 (2018).
 79. W. Nie, H. Tsai, R. Asadpour, J.-C. Blancon, A. J. Neukirch, G. Gupta, J. J. Crochet, M. Chhowalla, S. Tretiak, M. A. Alam, H.-L. Wang, and A. D. Mohite, "High-efficiency solution-processed perovskite solar cells with millimeter-scale grains," *Science* **347**, 522–525 (2015).
 80. X. Li, D. Bi, C. Yi, J.-D. Décoppet, J. Luo, S. M. Zakeeruddin, A. Hagfeldt, and M. Grätzel, "A vacuum flash–assisted solution process for high-efficiency large-area perovskite solar cells," *Science* **353**, 58–62 (2016).
 81. J.-W. Lee, H.-S. Kim, and N.-G. Park, "Lewis acid–base adduct approach for high efficiency perovskite solar cells," *Acc. Chem. Res.* **49**, 311–319 (2016).
 82. N. J. Jeon, J. H. Noh, Y. C. Kim, W. S. Yang, S. Ryu, and S. I. Seok, "Solvent engineering for high-performance inorganic–organic hybrid perovskite solar cells," *Nat. Mater.* **13**, 897–903 (2014).
 83. Q. Chen, H. Zhou, Z. Hong, S. Luo, H.-S. Duan, H.-H. Wang, Y. Liu, G. Li, and Y. Yang, "Planar heterojunction perovskite solar cells via vapor-assisted solution process," *J. Am. Chem. Soc.* **136**, 622–625 (2014).
 84. D. Bi, C. Yi, J. Luo, J.-D. Décoppet, F. Zhang, S. M. Zakeeruddin, X. Li, A. Hagfeldt, and M. Grätzel, "Polymer-templated nucleation and crystal growth of perovskite films for solar cells with efficiency greater than 21%," *Nat. Energy* **1**, 16142 (2016).
 85. L. Dou, Y. Yang, J. You, Z. Hong, W.-H. Chang, G. Li, and Y. Yang, "Solution-processed hybrid perovskite photodetectors with high detectivity," *Nat. Commun.* **5**, 5404 (2014).
 86. S. V. N. Pammi, R. Maddaka, V.-D. Tran, J.-H. Eom, V. Pecunia, S. Majumder, M.-D. Kim, and S. G. Yoon, "CVD-deposited hybrid lead halide perovskite films for high-responsivity, self-powered photodetectors with enhanced photo stability under ambient conditions," *Nano Energy* **74**, 104872 (2020).
 87. X. Liu, Z. Liu, J. Li, X. Tan, B. Sun, H. Fang, S. Xi, T. Shi, Z. Tang, and G. Liao, "Ultrafast, self-powered and charge-transport-layer-free photodetectors based on high-quality evaporated CsPbBr_3 perovskites for applications in optical communication," *J. Mater. Chem. C* **8**, 3337–3350 (2020).
 88. C. Bao, J. Yang, S. Bai, W. Xu, Z. Yan, Q. Xu, J. Liu, W. Zhang, and F. Gao, "High performance and stable all-inorganic metal halide perovskite-based photodetectors for optical communication applications," *Adv. Mater.* **30**, 1803422 (2018).
 89. L. Li, F. Zhang, S. Ye, X. Peng, Z. Sun, J. Lian, L. Liu, J. Qu, and J. Song, "Self-powered photodetectors based on $\text{Cs}_x\text{DMA}_{1-x}\text{PbI}_3$ perovskite films with high detectivity and stability," *Nano Energy* **71**, 104611 (2020).
 90. T. Pang, R. Jia, Y. Wang, K. Sun, Z. Hu, Y. Zhu, S. Luan, and Y. Zhang, "Self-powered behavior based on the light-induced self-poling effect in perovskite-based transport layer-free photodetectors," *J. Mater. Chem. C* **7**, 609–616 (2019).
 91. Y. Deng, Z. Xiao, and J. Huang, "Light-induced self-poling effect on organometal trihalide perovskite solar cells for increased device efficiency and stability," *Adv. Energy Mater.* **5**, 1500721 (2015).
 92. Y. Yuan, J. Chae, Y. Shao, Q. Wang, Z. Xiao, A. Centrone, and J. Huang, "Photovoltaic switching mechanism in lateral structure hybrid perovskite solar cells," *Adv. Energy Mater.* **5**, 1500615 (2015).
 93. L. Su, Z. X. Zhao, H. Y. Li, J. Yuan, Z. L. Wang, G. Z. Cao, and G. Zhu, "High-performance organolead halide perovskite-based self-powered triboelectric photodetector," *ACS Nano* **9**, 11310–11316 (2015).
 94. V. K. S. Hsiao, S.-F. Leung, Y.-C. Hsiao, P.-K. Kung, Y.-C. Lai, Z.-H. Lin, K. N. Salama, H. N. Alshareef, Z. L. Wang, and J.-H. He, "Photo-carrier extraction by triboelectricity for carrier transport layer-free photodetectors," *Nano Energy* **65**, 103958 (2019).
 95. O. Game, U. Singh, T. Kumari, A. Banpurkar, and S. Ogale, "ZnO (N)–Spiro-MeOTAD hybrid photodiode: an efficient self-powered fast-response UV (visible) photosensor," *Nanoscale* **6**, 503–513 (2014).
 96. C. Li, C. Han, Y. Zhang, Z. Zang, M. Wang, X. Tang, and J. Du, "Enhanced photoresponse of self-powered perovskite photodetector based on ZnO nanoparticles decorated CsPbBr_3 films," *Sol. Energy Mater. Sol. Cells* **172**, 341–346 (2017).
 97. F. Bai, J. Qi, F. Li, Y. Fang, W. Han, H. Wu, and Y. Zhang, "A high-performance self-powered photodetector based on monolayer MoS_2 /perovskite heterostructures," *Adv. Mater. Interfaces* **5**, 1701275 (2018).
 98. R. Saraf and V. Maheshwari, "Self-powered photodetector based on electric-field-induced effects in MAPbI_3 perovskite with improved stability," *ACS Appl. Mater. Interfaces* **10**, 21066–21072 (2018).
 99. M. Xue, H. Zhou, G. Ma, L. Yang, Z. Song, J. Zhang, and H. Wang, "Investigation of the stability for self-powered CsPbBr_3 perovskite photodetector with an all-inorganic structure," *Sol. Energy Mater. Sol. Cells* **187**, 69–75 (2018).
 100. Z.-X. Zhang, Z. Long-Hui, X.-W. Tong, Y. Gao, C. Xie, Y. H. Tsang, L.-B. Luo, and Y.-C. Wu, "Ultrafast, self-driven, and air-stable photodetectors based on multilayer PtSe_2 /perovskite heterojunctions," *J. Phys. Chem. Lett.* **9**, 1185–1194 (2018).
 101. U. Bansode, A. Rahman, and S. Ogale, "Low-temperature processing of optimally polymer-wrapped α - CsPbI_3 for self-powered flexible photo-detector application," *J. Mater. Chem. C* **7**, 6986–6996 (2019).
 102. J. Ghosh, G. Natu, and P. K. Giri, "Plasmonic hole-transport-layer enabled self-powered hybrid perovskite photodetector using a modified perovskite deposition method in ambient air," *Org. Electron.* **71**, 175–184 (2019).
 103. S. Murali, S. P. Madhusudanan, A. K. Pathak, P. M. Jayasankar, and S. K. Batabyal, "Carbon assisted methylammonium lead iodide microcrystalline device for an inexpensive self-powered photodetector," *Mater. Lett.* **254**, 428–432 (2019).
 104. X.-W. Tong, Z.-X. Zhang, D. Wang, L.-B. Luo, C. Xie, and Y.-C. Wu, "Inorganic $\text{CsBi}_3\text{I}_{10}$ perovskite/silicon heterojunctions for sensitive, self-driven and air-stable NIR photodetectors," *J. Mater. Chem. C* **7**, 863–870 (2019).
 105. L.-H. Zeng, Q.-M. Chen, Z.-X. Zhang, D. Wu, H. Yuan, Y.-Y. Li, W. Qarony, S. P. Lau, L.-B. Luo, and Y. H. Tsang, "Multilayered PdSe_2 /perovskite Schottky junction for fast, self-powered, polarization-sensitive, broadband photodetectors, and image sensor application," *Adv. Sci.* **6**, 1901134 (2019).
 106. W. Zhu, M. Deng, Z. Zhang, D. Chen, H. Xi, J. Chang, J. Zhang, C. Zhang, and Y. Hao, "Intermediate phase halide exchange strategy toward a high-quality, thick CsPbBr_3 film for optoelectronic applications," *ACS Appl. Mater. Interfaces* **11**, 22543–22549 (2019).
 107. G. R. Adams, V. O. Eze, M. A. S. Shohag, R. Simpson, H. Parker, and O. I. Okoli, "Fabrication of rapid response self-powered

- photodetector using solution-processed triple cation lead-halide perovskite," *Eng. Res. Express* **2**, 015043 (2020).
108. Z. Liu, X. Liu, B. Sun, X. Tan, H. Ye, J. Zhou, Z. Tang, T. Shi, and G. Liao, "Cu-doping strategy to enhance photoelectric performance of self-powered hole-conductor-free perovskite photodetector for optical communication applications," *Adv. Mater. Technol.* **5**, 2000260 (2020).
 109. M. I. Saleem, S. Yang, R. Zhi, H. Li, M. Sulaman, P. V. Chandrasekar, Z. Zhang, A. Batool, and B. Zou, "Self-powered, all-solution processed, trilayer heterojunction perovskite-based photodetectors," *Nanotechnology* **31**, 254001 (2020).
 110. W. Tian, L. Min, F. Cao, and L. Li, "Nested inverse opal perovskite toward superior flexible and self-powered photodetection performance," *Adv. Mater.* **32**, 1906974 (2020).
 111. Z. Zhang, W. Zhang, Q. Jiang, Z. Wei, M. Deng, D. Chen, W. Zhu, J. Zhang, and H. You, "Toward high-performance electron/hole-transporting-layer-free, self-powered CsPbI₂Br₂ photodetectors via interfacial engineering," *ACS Appl. Mater. Interfaces* **12**, 6607–6614 (2020).
 112. W. Zhu, M. Deng, D. Chen, D. Chen, H. Xi, J. Chang, J. Zhang, C. Zhang, and Y. Hao, "Sacrificial additive-assisted film growth endows self-powered CsPbBr₃ photodetectors with ultra-low dark current and high sensitivity," *J. Mater. Chem. C* **8**, 209–218 (2020).
 113. H. Fang, Q. Li, J. Ding, N. Li, H. Tian, L. Zhang, T. Ren, J. Dai, L. Wang, and Q. Yan, "A self-powered organolead halide perovskite single crystal photodetector driven by a DVD-based triboelectric nanogenerator," *J. Mater. Chem. C* **4**, 630–636 (2016).
 114. S.-T. Han, H. Peng, Q. Sun, S. Venkatesh, K.-S. Chung, S. C. Lau, Y. Zhou, and V. A. L. Roy, "An overview of the development of flexible sensors," *Adv. Mater.* **29**, 1700375 (2017).
 115. A. Manekkathodi, M.-Y. Lu, C. W. Wang, and L.-J. Chen, "Direct growth of aligned zinc oxide nanorods on paper substrates for low-cost flexible electronics," *Adv. Mater.* **22**, 4059–4063 (2010).
 116. W. Zheng, R. Lin, Z. Zhang, Q. Liao, J. Liu, and F. Huang, "An ultra-fast-temporally-responsive flexible photodetector with high sensitivity based on high-crystallinity organic-inorganic perovskite nanoflake," *Nanoscale* **9**, 12718–12726 (2017).
 117. C. Xie and F. Yan, "Flexible photodetectors based on novel functional materials," *Small* **13**, 1701822 (2017).
 118. Z. Liu, K. Parvez, R. Li, R. Dong, X. Feng, and K. Müllen, "Transparent conductive electrodes from graphene/PEDOT:PSS hybrid inks for ultrathin organic photodetectors," *Adv. Mater.* **27**, 669–675 (2015).
 119. K. Rana, J. Singh, and J.-H. Ahn, "A graphene-based transparent electrode for use in flexible optoelectronic devices," *J. Mater. Chem. C* **2**, 2646–2656 (2014).
 120. C. Bao, W. Zhu, J. Yang, F. Li, S. Gu, Y. Wang, T. Yu, J. Zhu, Y. Zhou, and Z. Zou, "Highly flexible self-powered organolead trihalide perovskite photodetectors with gold nanowire networks as transparent electrodes," *ACS Appl. Mater. Interfaces* **8**, 23868–23875 (2016).
 121. M. Vosgueritchian, D. J. Lipomi, and Z. Bao, "Highly conductive and transparent PEDOT:PSS films with a fluorosurfactant for stretchable and flexible transparent electrodes," *Adv. Funct. Mater.* **22**, 421–428 (2012).
 122. C. Perumal Veeramalai, S. Yang, J. Wei, M. Sulaman, R. Zhi, M. I. Saleem, Y. Tang, Y. Jiang, and B. Zou, "Porous single-wall carbon nanotube templates decorated with all-inorganic perovskite nanocrystals for ultraflexible photodetectors," *ACS Appl. Nano Mater.* **3**, 459–467 (2020).
 123. G. Cen, Y. Liu, C. Zhao, G. Wang, Y. Fu, G. Yan, Y. Yuan, C. Su, Z. Zhao, and W. Mai, "Atomic-layer deposition-assisted double-side interfacial engineering for high-performance flexible and stable CsPbBr₃ perovskite photodetectors toward visible light communication applications," *Small* **15**, 1902135 (2019).
 124. D. H. Shin, S. H. Shin, S. G. Lee, S. Kim, and S.-H. Choi, "High-detectivity/speed flexible and self-powered graphene quantum dots/perovskite photodiodes," *ACS Sustain. Chem. Eng.* **7**, 19961–19968 (2019).
 125. F. Cao, W. Tian, M. Wang, H. Cao, and L. Li, "Semitransparent, flexible, and self-powered photodetectors based on ferroelectricity-assisted perovskite nanowire arrays," *Adv. Funct. Mater.* **29**, 1901280 (2019).
 126. F. Cao, W. Tian, L. Meng, M. Wang, and L. Li, "Ultra-high-performance flexible and self-powered photodetectors with ferroelectric P(VDF-TrFE)/perovskite bulk heterojunction," *Adv. Funct. Mater.* **29**, 1808415 (2019).
 127. H. Sun, T. Lei, W. Tian, F. Cao, J. Xiong, and L. Li, "Self-powered, flexible, and solution-processable perovskite photodetector based on low-cost carbon cloth," *Small* **13**, 1701042 (2017).
 128. K. Shen, H. Xu, X. Li, J. Guo, S. Sathasivam, M. Wang, A. Ren, K. L. Choy, I. P. Parkin, Z. Guo, and J. Wu, "Flexible and self-powered photodetector arrays based on all-inorganic CsPbBr₃ quantum dots," *Adv. Mater.* **32**, 2000004 (2020).
 129. S.-F. Leung, K.-T. Ho, P.-K. Kung, V. K. S. Hsiao, H. N. Alshareef, Z. L. Wang, and J.-H. He, "A self-powered and flexible organometallic halide perovskite photodetector with very high detectivity," *Adv. Mater.* **30**, 1704611 (2018).
 130. H. Lu, W. Tian, F. Cao, Y. Ma, B. Gu, and L. Li, "A self-powered and stable all-perovskite photodetector-solar cell nanosystem," *Adv. Funct. Mater.* **26**, 1296–1302 (2016).
 131. D. Wu, H. Zhou, Z. Song, M. Zheng, R. Liu, X. Pan, H. Wan, J. Zhang, H. Wang, X. Li, and H. Zeng, "Welding perovskite nanowires for stable, sensitive, flexible photodetectors," *ACS Nano* **14**, 2777–2787 (2020).
 132. S. Lim, M. Ha, Y. Lee, and H. Ko, "Large-area, solution-processed, hierarchical MAPbI₃ nanoribbon arrays for self-powered flexible photodetectors," *Adv. Opt. Mater.* **6**, 1800615 (2018).
 133. M. Wang, F. Cao, L. Meng, W. Tian, and L. Li, "High-performance flexible self-powered photodetector based on perovskite and low-temperature processed In₂S₃ nanoflake film," *Adv. Mater. Interfaces* **6**, 1801526 (2019).
 134. J. M. Kim, D. H. Shin, and S.-H. Choi, "Highly-flexible perovskite photodiodes employing doped multilayer-graphene transparent conductive electrodes," *Nanotechnology* **29**, 425203 (2018).
 135. J. M. Kim, S. Kim, and S.-H. Choi, "High-performance n-i-p-type perovskite photodetectors employing graphene-transparent conductive electrodes N-type doped with amine group molecules," *ACS Sustain. Chem. Eng.* **7**, 734–739 (2019).
 136. H. Sun, W. Tian, F. Cao, J. Xiong, and L. Li, "Ultra-high-performance self-powered flexible double-twisted fibrous broadband perovskite photodetector," *Adv. Mater.* **30**, 1706986 (2018).
 137. X.-D. Wang, W.-G. Li, J.-F. Liao, and D.-B. Kuang, "Recent advances in halide perovskite single-crystal thin films: fabrication methods and optoelectronic applications," *Sol. RRL* **3**, 1800294 (2019).
 138. B. Paci, A. Generosi, J. Wright, C. Ferrero, D. A. Carlo, and F. Brunetti, "Planar perovskite solar cells: local structure and stability issues," *Sol. RRL* **1**, 1700066 (2017).
 139. T.-B. Song, Q. Chen, H. Zhou, C. Jiang, H.-H. Wang, Y. Yang, Y. Liu, J. You, and Y. Yang, "Perovskite solar cells: film formation and properties," *J. Mater. Chem. A* **3**, 9032–9050 (2015).
 140. Z. Xiao, Y. Yuan, Q. Wang, Y. Shao, Y. Bai, Y. Deng, Q. Dong, M. Hu, C. Bi, and J. Huang, "Thin-film semiconductor perspective of organometal trihalide perovskite materials for high-efficiency solar cells," *Mater. Sci. Eng. R* **101**, 1–38 (2016).
 141. I. C. Smith, E. T. Hoke, D. Solis-Ibarra, M. D. McGehee, and H. I. Karunadasa, "A layered hybrid perovskite solar-cell absorber with enhanced moisture stability," *Angew. Chem.* **53**, 11232–11235 (2014).
 142. C. C. Stoumpos, C. D. Malliakas, and M. G. Kanatzidis, "Semiconducting tin and lead iodide perovskites with organic cations: phase transitions, high mobilities, and near-infrared photoluminescent properties," *Inorg. Chem.* **52**, 9019–9038 (2013).
 143. C. Ran, J. Xu, W. Gao, C. Huang, and S. Dou, "Defects in metal triiodide perovskite materials towards high-performance solar cells: origin, impact, characterization, and engineering," *Chem. Soc. Rev.* **47**, 4581–4610 (2018).
 144. Q. Wang, B. Chen, Y. Liu, Y. Deng, Y. Bai, Q. Dong, and J. Huang, "Scaling behavior of moisture-induced grain degradation in

- polycrystalline hybrid perovskite thin films," *Energy Environ. Sci.* **10**, 516–522 (2017).
145. J. H. Noh, S. H. Im, J. H. Heo, T. N. Mandal, and S. I. Seok, "Chemical management for colorful, efficient, and stable inorganic–organic hybrid nanostructured solar cells," *Nano Lett.* **13**, 1764–1769 (2013).
146. B. Conings, J. Drijkoningen, N. Gauquelin, A. Babayigit, J. D'Haen, L. D'Olieslaeger, A. Ethirajan, J. Verbeeck, J. Manca, E. Mosconi, F. D. Angelis, and H.-G. Boyen, "Intrinsic thermal instability of methylammonium lead trihalide perovskite," *Adv. Energy Mater.* **5**, 1500477 (2015).
147. C. L. C. Ellis, H. Javaid, E. C. Smith, and D. Venkataraman, "Hybrid perovskites with larger organic cations reveal autocatalytic degradation kinetics and increased stability under light," *Inorg. Chem.* **59**, 12176–12186 (2020).
148. W. Nie, J.-C. Blancon, A. J. Neukirch, K. Appavoo, H. Tsai, M. Chhowalla, M. A. Alam, M. Y. Sfeir, C. Katan, J. Even, S. Tretiak, J. J. Crochet, G. Gupta, and A. D. Mohite, "Light-activated photocurrent degradation and self-healing in perovskite solar cells," *Nat. Commun.* **7**, 11574 (2016).
149. S. Ito, S. Tanaka, K. Manabe, and H. Nishino, "Effects of surface blocking layer of Sb_2S_3 on nanocrystalline TiO_2 for $\text{CH}_3\text{NH}_3\text{PbI}_3$ perovskite solar cells," *J. Phys. Chem. C* **118**, 16995–17000 (2014).
150. Z. Song, C. Wang, A. B. Phillips, C. R. Grice, D. Zhao, Y. Yu, C. Chen, C. Li, X. Yin, R. J. Ellingson, M. J. Heben, and Y. Yan, "Probing the origins of photodegradation in organic–inorganic metal halide perovskites with time-resolved mass spectrometry," *Sustain. Energy Fuels* **2**, 2460–2467 (2018).
151. M. Bag, L. A. Renne, R. Y. Adhikari, S. Karak, F. Liu, P. M. Lahti, T. P. Russell, M. T. Tuominen, and D. Venkataraman, "Kinetics of ion transport in perovskite active layers and its implications for active layer stability," *J. Am. Chem. Soc.* **137**, 13130–13137 (2015).
152. B. Hailegnaw, S. Kirmayer, E. Edri, G. Hodes, and D. Cahen, "Rain on methylammonium lead iodide based perovskites: possible environmental effects of perovskite solar cells," *J. Phys. Chem. Lett.* **6**, 1543–1547 (2015).
153. F. Giustino and H. J. Snaith, "Toward lead-free perovskite solar cells," *ACS Energy Lett.* **1**, 1233–1240 (2016).
154. Z. Shi, J. Guo, Y. Chen, Q. Li, Y. Pan, H. Zhang, Y. Xia, and W. Huang, "Lead-free organic–inorganic hybrid perovskites for photovoltaic applications: recent advances and perspectives," *Adv. Mater.* **29**, 1605005 (2017).
155. M. Wang, W. Wang, B. Ma, W. Shen, L. Liu, K. Cao, S. Chen, and W. Huang, "Lead-free perovskite materials for solar cells," *Nano-Micro Lett.* **13**, 62 (2021).
156. N. K. Noel, S. D. Stranks, A. Abate, C. Wehrenfennig, S. Guarnera, A.-A. Haghighirad, A. Sadhanala, G. E. Eperon, S. K. Pathak, M. B. Johnston, A. Petrozza, L. M. Herz, and H. J. Snaith, "Lead-free organic–inorganic tin halide perovskites for photovoltaic applications," *Energy Environ. Sci.* **7**, 3061–3068 (2014).
157. N. Leblanc, N. Mercier, L. Zorina, S. Simonov, P. Auban-Senzier, and C. Pasquier, "Large spontaneous polarization and clear hysteresis loop of a room-temperature hybrid ferroelectric based on mixed-halide $[\text{BiI}_3\text{Cl}_2]$ polar chains and methylviologen dication," *J. Am. Chem. Soc.* **133**, 14924–14927 (2011).
158. W. Bi, N. Leblanc, N. Mercier, P. Auban-Senzier, and C. Pasquier, "Thermally induced Bi(III) lone pair stereoactivity: ferroelectric phase transition and semiconducting properties of $(\text{MV})\text{BiBr}_5$ (MV = methylviologen)," *Chem. Mater.* **21**, 4099–4101 (2009).
159. B.-W. Park, B. Philippe, X. Zhang, H. Rensmo, G. Boschloo, and E. M. J. Johansson, "Bismuth based hybrid perovskites A_3BiI_9 (A: methylammonium or cesium) for solar cell application," *Adv. Mater.* **27**, 6806–6813 (2015).
160. T. Krishnamoorthy, H. Ding, C. Yan, W. L. Leong, T. Baikie, Z. Zhang, M. Sherburne, S. Li, M. Asta, N. Mathews, and S. G. Mhaisalkar, "Lead-free germanium iodide perovskite materials for photovoltaic applications," *J. Mater. Chem. A* **3**, 23829–23832 (2015).